Transportation Research Part C 125 (2021) 103012

Contents lists available at ScienceDirect

Transportation Research Part C

journal homepage: www.elsevier.com/locate/trc

Bicycle flow dynamics on wide roads: Experiments and simulation

Ning Guo [a], Rui Jiang [b,*], SC Wong [c,*], Qing-Yi Hao [d], Shu-Qi Xue [e], Mao-Bin Hu [f]

[a] School of Automotive and Transportation Engineering, Hefei University of Technology, Hefei 230009, PR China
[b] Key Laboratory of Transport Industry of Big Data Application Technologies for Comprehensive Transport, Ministry of Transport, Beijing Jiaotong University, Beijing 100044, PR China
[c] Department of Civil Engineering, The University of Hong Kong, Pokfulam Road, Hong Kong, PR China
[d] School of Mathematics and Computational Science, Anqing Normal University, Anqing 246133, PR China
[e] School of Modern Posts, Xian University of Posts and Telecommunications, 710061 Xi'an, PR China
[f] School of Engineering Science, University of Science and Technology of China, Hefei 230026, PR China

ARTICLE INFO

Keywords:
Bicycle flow
Experiments
Fundamental diagram
Stop-and-go waves
Heuristic-based model
Centrifugal effect

ABSTRACT

Cycling is a popular and sustainable mode of transportation. However, few studies have examined experimental and modeling studies on bicycle flow dynamics. In particular, for wide roads, the characteristics of high-density regimes in the fundamental diagram have not been well addressed, and the emergence of stop-and-go waves has not been fully understood. This study experimentally investigated bicycle flow dynamics on wide roads, using two types of 3-m-wide track. Different riding behaviors, namely, free riding, following, and overtaking, were analyzed. The bicycle flow dynamics were found to be essentially the same on the two tracks: (i) The bicycle flow rate remained nearly constant across a wide range of densities, in marked contrast to the single-file bicycle flow, which exhibited a unimodal fundamental diagram. By studying the weight density of the radial and lateral locations of cyclists, we argue that this behavior arises from the formation of more lanes with increase in global density. The newly formed lanes prevented the flow rate from decreasing. (ii) When the density exceeded 0.5 bicycles/m^2, the flow rate began to decrease, and stop-and-go traffic emerged. Based on these behavioral observations, we propose an improved heuristic-based model to simulate bicycle flow on roads of different radii and explicitly account for the centrifugal effect of bicycles. The calibration and validation results demonstrate that the proposed model can reproduce the traffic dynamics of bicycle flow.

1. Introduction

Economic development and population growth have placed tremendous pressure on urban transportation systems, especially in developing countries like China. The reliance on private cars for travel has had severe negative effects, such as traffic congestion and air and noise pollution. Government transportation departments now face the challenge of promoting environmentally friendly and physically active transportation modes. To this end, transportation management strategies often encourage cycling for both commuting and short utilitarian trips (Maibach et al., 2009; Rojas-Rueda et al., 2011). Cycling has the potential to reduce air pollution and mitigate climate change while offering individuals a low-cost travel option that benefits their personal health and fitness (Wen and Rissel, 2008; World Health Organization, 2009; 2011; Yang and Zacharias, 2016; Mueller et al., 2018; Doorley et al., 2020).

* Corresponding authors.
E-mail addresses: jiangrui@bjtu.edu.cn (R. Jiang), hhecwsc@hku.hk (S. Wong).

https://doi.org/10.1016/j.trc.2021.103012
Received 2 September 2020; Received in revised form 1 February 2021; Accepted 3 February 2021
Available online 18 February 2021

Cycling has become an important transportation mode in urban life. Many governments have advocated cycling by adopting pro-bicycle measures, such as bicycle-exclusive road networks and full integration with public transportation. Cycling can be faster than other forms of transport for short or even medium-distance trips (Zahabi et al., 2016; Campbell et al., 2016). As a result, bicycles have become particularly important in some countries. For example, bicycle trips account for 10% of overall transport in Germany and Sweden, 11% in Finland, 18% in Denmark, and 27% in the Netherlands (Pucher and Buehler, 2008). In China, congestion in Beijing, Shenzhen, and Guangzhou has dropped by 7.4%, 6.8%, and 4.1%, respectively, due to bicycle sharing[1].

To better manage bicycle transport in urban areas, it is essential to understand the traffic dynamics of bicycle flow. There are generally two approaches to study bicycle dynamics: field observations and controlled experiments. Some findings based on field observations have been reported regarding bicycle road capacity (Homburger, 1976; Botma and Papendrecht, 1991; Raksuntorn and Khan, 2003), flow rate versus density (Navin, 1994; Li et al., 2015; Jin et al., 2017), and cyclist behavior (Paulsen et al., 2019; Mohammed et al., 2019). For example, bicycle capacity was found to be approximately 2600 bicycles/hr/m (lane width = 1 m) in Davis, California (USA) (Homburger, 1976), and 3850–4480 bicycles/hr/m (lane width = 0.78 m) in the Netherlands (Botma and Papendrecht, 1991). Raksuntorn and Khan (2003) showed a maximum flow rate of 1875 bicycles/hr/m (lane width = 0.78 m) at the stop line of signalized intersections. Li et al. (2015) found that bicycle speed and speed variation decrease with increasing density and that the overtaking probability is highest for densities of 150 bicycles/km/lane. Paulsen et al. (2019) observed forced-following behavior, where faster cyclists are delayed by slower ones in moderate traffic flows. From the video at the Brooklyn Bridge, New York City, Mohammed et al. (2019) found that all the longitudinal distance, lateral distance and speed difference between cyclists have potential effect on the following or overtaking choice. The following interactions of cyclists include constrained and unconstrained states. The overtaking interactions include initiation, merging and post-overtaking states.

The external environment in field observations is often complex and uncontrollable, which complicates the analysis of how different factors contribute to flow dynamics. In contrast, experimental studies are more controllable and exclude certain complicated factors, and have therefore become a powerful tool to study the traffic flow of vehicles, pedestrians, and bicycles. Several experiments have reported bicycle dynamics on single-file tracks. Mai et al. (2012) and Jiang et al. (2017) performed a single-file bicycle flow experiment on a 146-m playground-like road, extracted the trajectories of each bicycle, and presented a fundamental diagram. Their results show that single-file flow exhibits a unimodal fundamental diagram, and that traffic jams spontaneously form above a critical density of $\rho \approx 0.37$ bicycles/m. Zhang et al. (2014) performed a similar single-file bicycle experiment on an 86-m track and found that the flow rate dropped sharply at $\rho = 0.3$ bicycles/m, marking the transition into a congested state, and observed stop-and-go waves when $\rho = 0.384$ bicycles/m, which is very similar to the critical value reported in Jiang et al. (2017). Zhao and Zhang (2017) also conducted single-file experiments for bicycles on a 52-m circular track and compared single-file experiments involving cars, pedestrians, and bicycles, yielding very similar results to those of Jiang et al. (2017) and Zhang et al. (2014).

In the abovementioned single-file experimental studies, bicycles were not allowed to overtake each other, and the allowed behavior was restricted to bicycle-following, which is usually not the case in real bicycle flow on wide roads where cyclists commonly follow, ride side-by-side, zipper, or overtake a leading cyclist. A limited number of studies have investigated bicycle flow on wide roads that allow all of these behaviors. Gavriilidou et al. (2019a, 2019b) designed a wide-track experiment to investigate the service level of bicycle facilities. They found that many cyclists choose to overtake on curves rather than on straight roads, and that cyclists prefer steering and following at low speed to maintain space over stopping. Wierbos et al. (2019) performed an experiment to investigate bicycle flow through a bottleneck with a single rectangle obstacle set on a 3 m-wide straight road. They found that traffic capacity increases linearly with bottleneck width and that a capacity reduction occurs after the onset of congestion. A staggered distribution forms when the bottleneck width is larger than 0.75 m and that only single-file movement can be observed when the bottleneck is $<$0.75-m wide.

Despite the abovementioned studies, bicycle flow dynamics on wide roads remain poorly understood and two fundamental issues have not been well addressed: (1) At high densities, what is the relationship between density, speed, and rate of bicycle flow on wide roads? How is the relationship similar to or different from that of single-file bicycle flow? (2) What are the bicycle flow dynamics on wide roads? Do stop-and-go waves emerge in wide-track bicycle flows at high densities? If so, what is the threshold density that is required for their emergence?

To address the two research questions, we conducted two sets of bicycle experiments on two types of 3-m-wide tracks. The experiments demonstrated that the flow rate on wide tracks remained nearly constant across a wide range of densities, in marked contrast to the single-file bicycle flow, which exhibited a unimodal fundamental diagram. Moreover, the flow rate began to decrease at densities higher than 0.5 bicycles/m^2, and stop-and-go traffic emerged. In addition, we propose a simulation model based on the behavioral analysis of riding behaviors. The proposed model can reproduce the observed characteristics of bicycle flow.

The paper is organized as follows. Section 2 presents our experimental setup. Section 3 presents experimental results and analysis. Section 4 proposes the heuristic-based model. Section 5 presents the model calibration. Section 6 presents the model validation. Conclusions are given in Section 7.

2. Experimental setup

To study the bicycle dynamics on wide roads, two sets of experiment were performed on two different types of 3-m-wide track. One

[1] https://www.chinadialogue.net/article/show/single/en/9853-Bike-sharing-schemes-Flourishing-or-running-riot- (accessed on July 24, 2020).

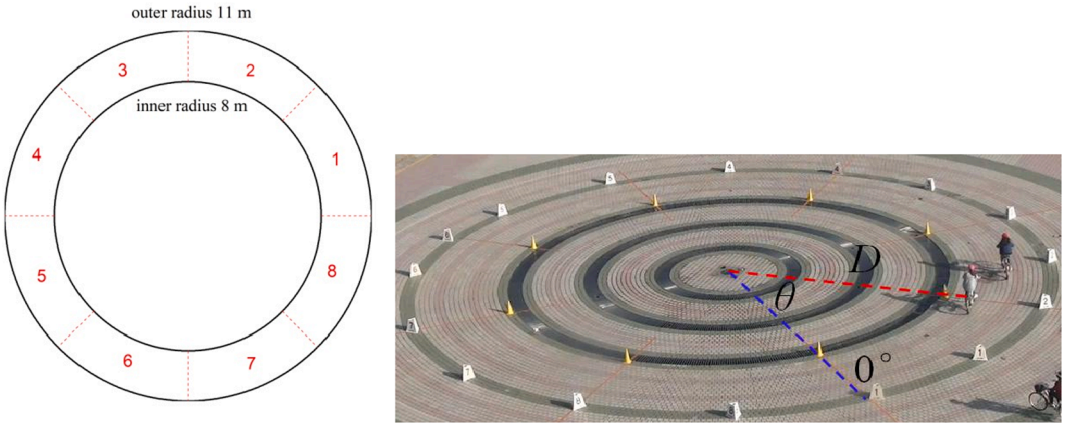

Fig. 1. Experimental field of the ring-shaped track. Left: schematic; Right: photograph.

Table 1
Serial numbers in each experimental run.

Run	Number of participants	Serial numbers
1	50	1–50
2	50	51–100
3	40	1–40
4	60	41–100
5	30	1–30
6	70	31–100
7	20	1–20
8	80	21–100
9	10	1–10
10	90	11–100
11	100	1–100

is a ring-shaped track with 8-m inner radius. The other is a playground-like track, which has two semicircles with 4-m inner radius joined by 13-m straight sections. By using these two tracks, bicycle flow data from two curvature radii can be obtained, i.e. small radius (4–7 m), and large radius (8–11 m).

Because of the absence of bottlenecks on the tracks, we choose two types of tracks to observe the endogenetic traffic flow dynamics. In the experiments, the control variable is the global density (i.e., number of bicycles divided by track area). By varying the global density, the flow rate can be measured at different densities, and the fundamental diagram can be obtained. Moreover, we can observe the spatiotemporal evolution of bicycle flow at different densities and examine whether stop-and-go traffic emerges.

2.1. Experiment set I: Multi bicycles on the ring-shaped track

The experiment was conducted on May 7, 2016, at Anqing Normal University (Anqing, China) on an artificial ring-shaped track with a periodic boundary to maintain the system density. The circular track was a standard test track used to study the traffic flow of pedestrians, cars, and bicycles (e.g., Moussaïd et al., 2012; Tadaki et al., 2013; Guo et al., 2016; Stern et al., 2018; Wu et al., 2019; Jin et al., 2019). The inner and outer radii of the track were 8 and 11 m, respectively, and the boundaries were marked with dark floor tiles, traffic cones, and number signs (Fig. 1). The number signs partitioned the track into eight uniform subareas for statistical purposes. The area of the experimental track was approximately 180 m^2. A total of 100 participants (30 male and 70 female undergraduate students) took part in the experiments. Each participant was assigned a serial number from 1 to 100 and requested to ride on the track in their usual manner. The participants were not informed of the experiments' objectives.

The full experimental procedure consisted of two rounds, each of which comprised 11 runs of experiments with different numbers of participants. Chronologically, the 11 runs involved the following number of participants: $N = 50, 50, 40, 60, 30, 70, 20, 80, 10, 90,$ and 100. The serial numbers were complementary between runs, as shown in Table 1. Except the last run, participants were assigned to perform experimental runs such that no participant performed two runs in succession. Therefore, each participant had a rest after one run. In each experimental run, the participants were initially randomly distributed on the track and requested to ride counterclockwise. Each run lasted at least 3 min. As the density increased, the time increased to 5 min and the bicycle flow ultimately reached a stationary state. The participants were provided sufficient time to rest after the first round of experiments before starting the second round. In the experiments, we observed that stop-and-go traffic emerged at the same density in both rounds. Therefore, we deemed that the experimental replications were adequate, and thus no further experimental rounds were conducted.

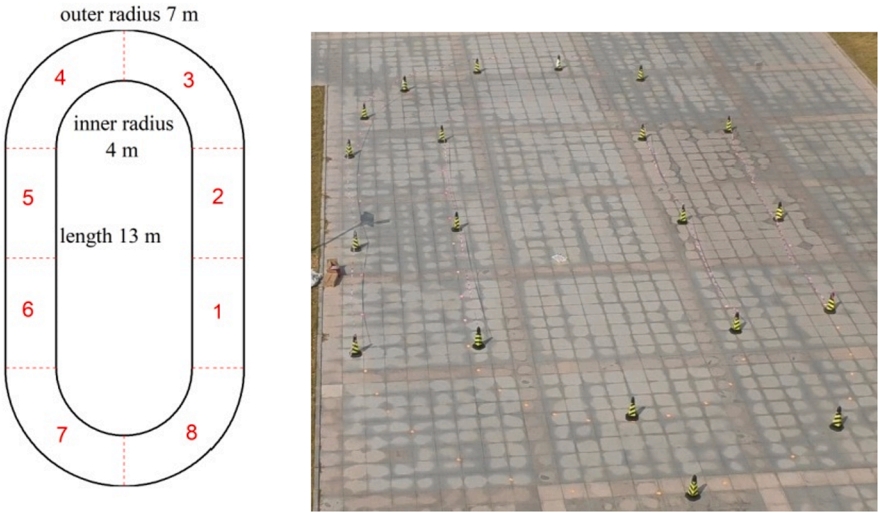

Fig. 2. Experimental field of the multi-circle track. Left: schematic; Right: snapshot.

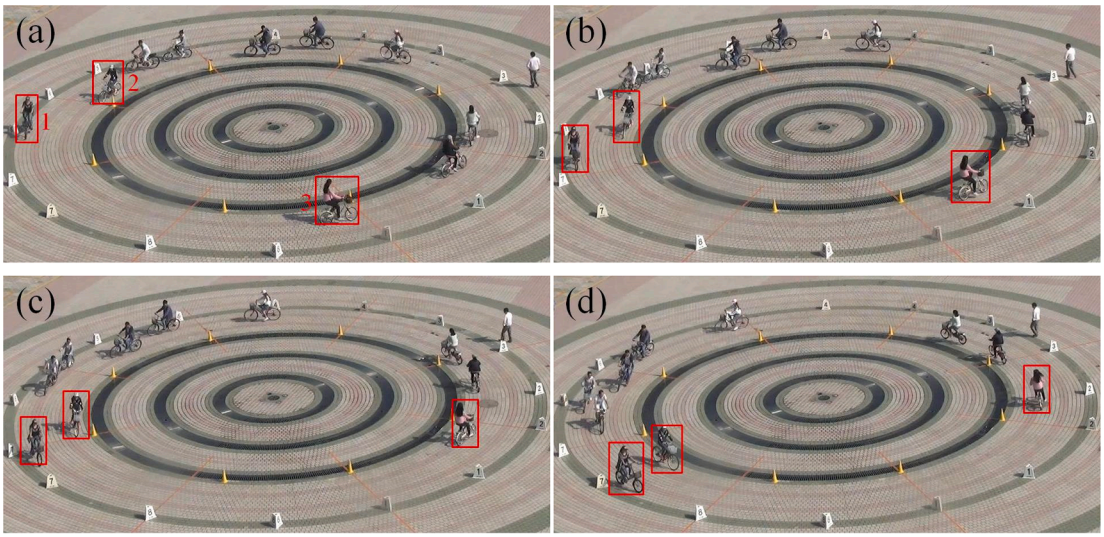

Fig. 3. Photographs of the 10-bicycle experiment.

A video camera (SONY HDR-CX510E) was used to film the experiments from the roof of a school building neighboring the track. The horizontal and vertical distances from the camera to the center of the ring-shaped track were 53 m and 24 m, respectively. The cyclists' heads were manually extracted using Tracker software (http://physlets.org/tracker/). The angle perpendicular to the camera was 65.4°, and the maximum height difference of cyclists was approximately 15 cm (160–175 cm). The maximum error was approximately 8 cm (Boltes and Seyfried, 2013).

2.2. *Experiment set II: Multi bicycles on the playground-like track*

Experiment set II was performed on September 28, 2019, at Anqing Normal University on an artificial playground-like track with a combination of straight and curve segments. The inner and outer radii of the semicircle segment were 4 and 7 m, respectively, and the two straight segments were both 13-m long. The boundaries were marked with traffic cones and color pasters (Fig. 2). The area of the experimental track was 180 m^2. A total of 100 participants (32 male and 68 female undergraduate students) took part in the experiments. Each participant was assigned a serial number from 1 to 100 and requested to ride on the track in their usual manner. The participants were not informed of the experiments' objectives.

The full experimental procedure consisted of two rounds, which were the same as in set I. Each round comprised 11 experimental runs with different numbers of participants. The serial numbers were also complementary between runs, as shown in Table 1. The initial distribution of cyclists and experiment run times were also similar to those in set I.

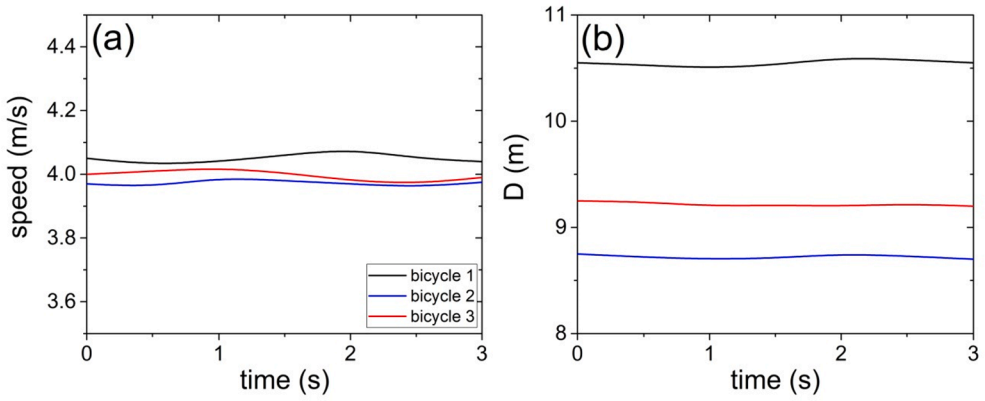

Fig. 4. Evolution in the 10-bicycle experiment: (a) speed, and (b) lateral location (polar radial distance *D*).

Fig. 5. Photographs of overtaking and following behaviors in the 40-bicycle experiment. The faster cyclist (red box) overtook slower cyclists. The focal cyclist (green box) followed those ahead.

A video camera (Panasonic HC-VX980) was used to film the experiment from the highest floor of a school building neighboring the track. The horizontal and vertical distances from the camera to the center of the playground-like track were 27 m and 20 m, respectively. The cyclists' heads were extracted using Petrack software (Boltes et al., 2010). The angle perpendicular to the camera was 53.5°, and the height range of cyclists is about 15 cm (160–175 cm). The maximum error is about 5.1 cm (Boltes et al., 2010).

3. Experimental results

3.1. Riding behaviors

Riding behaviors can be roughly classified into free-flow riding, following, and overtaking. For each of these three behaviors, the cyclists choose the riding direction and riding speed differently. At a low bicycle density, the cyclists were able to ride freely (see the photographs in Fig. 3). Fig. 4 shows the speed and lateral location of three bicycles. Evidently, the speed and lateral location were nearly constant over time, implying that the bicycles moved along the tangential direction of the ring. The free-flow speed was approximately 4 m/s, which is consistent with the free speeds recorded in other studies in China (~12–20 km/h) (Liu et al., 1993; Wei et al., 1997; Allen et al., 1998; Cherry, 2007; Lin et al., 2008; Jin et al., 2017).

The green boxes in Figs. 5 and 6 show typical following behavior at low and high densities, respectively. At a low density, the space ahead of the focal cyclist was sufficient for maintaining a high desired speed, so the focal cyclist followed the cyclist in front (Fig. 5). Note that although space to the right of the focal cyclist was available, the cyclist did not change direction. This indicates a direction preference behavior: cyclists prefer the target direction over changing direction. At a high bicycle density, all directions to overtake the cyclists ahead were blocked. Thus, the focal cyclist had no opportunity to overtake and had to follow the cyclist in front (Fig. 6).

Fig. 6. Photographs of following behavior in the 90-bicycle experiment. The focal cyclist (green box) followed those ahead.

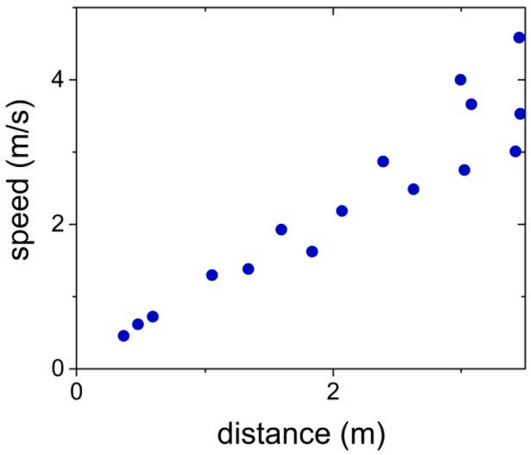

Fig. 7. Relationship between gap and speed during following behavior.

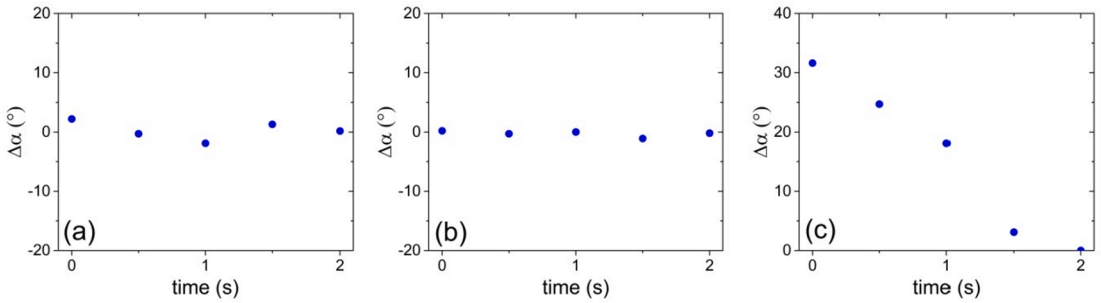

Fig. 8. Difference in the angle between the tangential direction and the movement direction (i.e., turning angle) for the cases presented in Figs. 5 and 6. (a) Following behavior at a low bicycle density, (b) following behavior at a high bicycle density, and (c) overtaking behavior.

During following behavior, speed is determined by the gap between cyclists. In each run, we randomly chose several bicycles that were exhibiting following behavior. We extracted the speed of and the gap between the bicycles. As shown in Fig. 7, speed was roughly proportional to the gap. The riding directions of the bicycles were usually along the tangential direction of the ring (Fig. 8a and 8b).

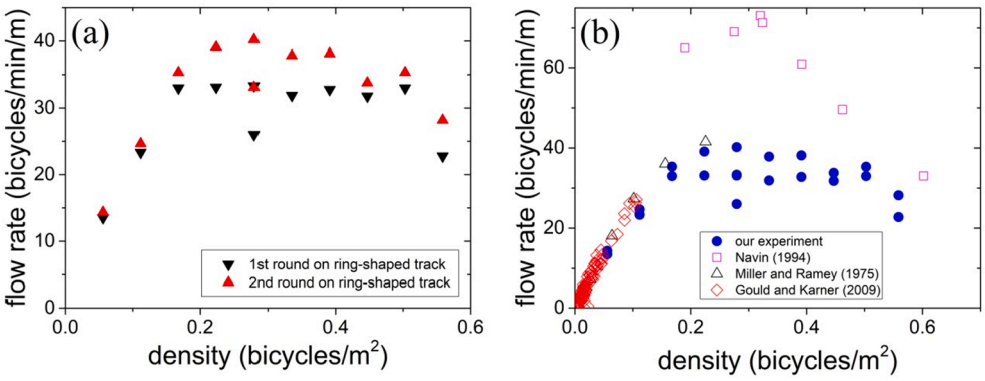

Fig. 9. Flow rate as a function of global density. (a) Our experiment; (b) Comparison with previous studies.

Table 2
Relative error in the flow rate between two rounds of experiment.

	N	10	20	30	40	50	60	70	80	90	100
Relative error (%)	1st round	−3.02	−2.78	−3.42	−8.29	−2.55/−4.52	−8.55	−7.56	−3.06	−3.42	−10.61
	2nd round	2.9	2.78	3.42	8.31	15.18/−5.51	8.53	7.54	3.04	3.40	10.60

Finally, we present an example of overtaking behavior, wherein a faster cyclist overtook slower cyclists (red box in Fig. 5). The faster cyclist successfully found a movement direction to actively bypass the other bicycles. The direction chosen was usually the most direct path to the cyclist's destination, after accounting for the presence of other bicycles. During typical overtaking, the bicycle had to turn sharply away from the tangential direction and then realign with the tangent direction after overtaking (Fig. 8c).

3.2. Fundamental diagram on wide tracks

We studied the fundamental diagram of flow rate versus global density to determine the effect of the number of bicycles on the system performance. The flow rate (q) is defined as the number of cyclists (N_c) crossing a line segment perpendicular to their direction of movement per unit time and per unit width.

$$q = N_c/[(T - T_d) \cdot w] \tag{1}$$

where $w = 3$ m is the width of the track and T is the experiment duration. The first $T_d = 0.5$ min of each experiment were excluded to discard transient time effects. We checked different cross sections and found that the flow rate was nearly the same.

Fig. 9a shows the fundamental diagram on the ring-shaped track. On this track, when the density was lower than 0.17 bicycles/m^2 (30 cyclists), the bicycles exhibited a free flow state, in which the flow rate increased with density. The flow rate then became nearly constant until the density reached 0.50 bicycles/m^2 (90 cyclists). In the 100-participant experiment, the flow rate began to decrease as the bicycle flow became congested. The existence of a constant flow across a wide range of densities gives rise to a trapezoidal fundamental diagram, which is markedly different from the unimodal diagram of single-file bicycle flow (Jiang et al., 2017).

The flow rates in the second round of experiments were typically higher than those in the first round. Table 2 shows the relative error in the flow rate, which was calculated as (sample value - average value)/average value. The maximum error was approximately 15%. A possible reason for this is the learning effect, as the participants were more familiar with the riding environment in the second round. There might also be a learning effect within a round. With 50 participants, the lowest flow rate corresponded to Run 1 in Round 1. This was most likely attributable to the participants' unfamiliarity with the track. Although runs 1 and 2 comprised the same number of participants, the groups comprised different participants. The density was different for the other runs in a round. These experimental settings make it difficult to quantify the within-round learning effect.

Fig. 9b compares the fundamental diagram with a selection of previously reported, empirically determined fundamental diagrams. Miller and Ramey (1975) and Gould and Karner (2009) investigated the relationship between flow rate and density on a public bicycle road and on a campus road, respectively. The low-density flow rates that they recorded were similar to those we observed in our experiment. However, the high-density flow data were absent at the observation sites. Navin (1994) conducted a bicycle experiment on a 4-m-wide oval track with participants who were aged 11–14 years. In each experimental run, all of the participants followed a lead cyclist, and maintained a safe and comfortable space from each other. The flow rate increased slowly from about 62 to 66 bicycles/min/m in the density interval 0.2–0.32 bicycles/m^2. Thereafter, the flow rate decreased rapidly to 32 bicycles/min/m when the density reached 0.6 bicycles/m^2. In contrast to the trapezoidal fundamental diagram in our experiment, Navin's experiment yielded a unimodal fundamental diagram. The flow rates recorded in their experiment were much higher than those in our experiment; in particular, the peak flow rate was approximately 60% higher. However, at high densities, this difference becomes smaller. These

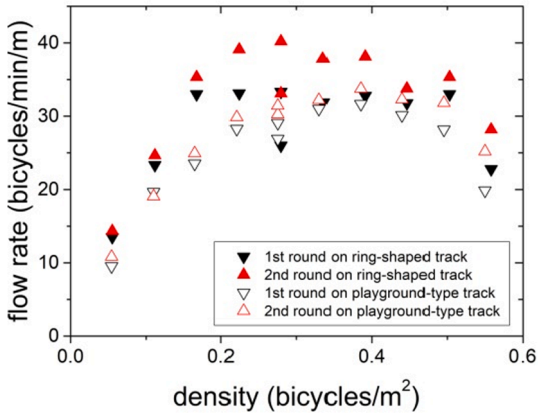

Fig. 10. Flow rate as a function of global density.

Table 3
Relative error in the flow rate between two rounds of experiment.

	N	10	20	30	40	50	60	70	80	90	100
Relative error (%)	1st round	−6.46	1.55	−2.89	−2.75	−8.56/−1.20	−1.93	−3.18	−3.45	−6.08	−11.83
	2nd round	6.45	−1.55	2.89	2.75	2.88/6.88	1.93	3.19	3.45	6.08	11.84

differences in results between the experiments are due to the different experimental settings. For example, in Navin's experiment, each group has only 12 participants, each test speed was predetermined and controlled by a lead cyclist, and the instruction was "to ride behind and fill in the space behind the pace setter at a spacing they considered safe and comfortable." Note that in their study, the largest predetermined speed is about 22 km/h, much higher than the free speed of bicycles in our experiment (approximately 15 km/h).

In other studies, although the fundamental diagram was not reported, the capacity was. The reported observed capacities vary but are roughly consistent with those in our experiment. For example, Raksuntorn and Khan (2003) collected data at the stop line of signalized intersections and reported a maximum flow rate of 31 bicycles/min/m. Similarly, the capacities in Beijing and Shanghai have been reported to be 35 bicycles/min/m (Xu, 1992; Liu et al., 1993), whereas a study in Davis, California (Homburger, 1976) reported a bicycle lane capacity of approximately 43 bicycles/min/m.

The fundamental diagram on the playground-like track is generally similar to that on the ring-shaped track. However, the wide range of constant flow rates is less apparent. Fig. 10 shows that the flow rate slowly increased with the density until reaching a global density of 0.275 bicycles/m^2 (50 cyclists). The flow rate was then approximately 30 bicycles/min/m until the density reached 0.495 bicycles/m^2 (90 cyclists, Fig. 10). The flow rates in the second round of experiments were also mostly higher than those in the first round. But the difference was not as significant as in experiment set I. Table 3 shows the relative error in the flow rate. The maximum error was approximately 10%. In the free flow state, the flow rate on the playground-like track was notably smaller than that on the ring-shaped track. This is because the free speed on the playground-like track (~3 m/s) is much smaller than that on ring-shaped track (~4 m/s). The reasons are as follows. (1) The curvature radius of the semicircle segment on the playground-like track is smaller than that of the ring-shaped track. From Appendix A, the free speed is about 2.5–3.5 m/s over the curvature radius interval 4–7 m, compared to approximately 3.3–4.2 m/s over the interval 8–11 m. (2) The cyclists did not accelerate too much on the straight track; thus, the free speed on the straight section was only slightly higher than that on the curved section. When the global density was larger than 0.4 bicycles/m^2, the flow rates on both tracks were similar because bicycles cannot move at free speed in the congestion state, and thus move at similar slow speeds.

To compare the bicycle flows on the curved and straight segments in set II, we analyze the fundamental diagram from the perspective of local measure. We extract the location of each participant $[x_i(t), y_i(t)]$, and the velocity of each participant is given as

$$v_i(t) = \frac{\sqrt{[x_i(t+\Delta t) - x_i(t-\Delta t)]^2 + [y_i(t+\Delta t) - y_i(t-\Delta t)]^2}}{2\Delta t} \tag{2}$$

where Δt is the step time (0.1 s). The local density $\rho_l(t)$ is

$$\rho_l(t) = \frac{N_l(t)}{S_l} \tag{3}$$

and the average speed is

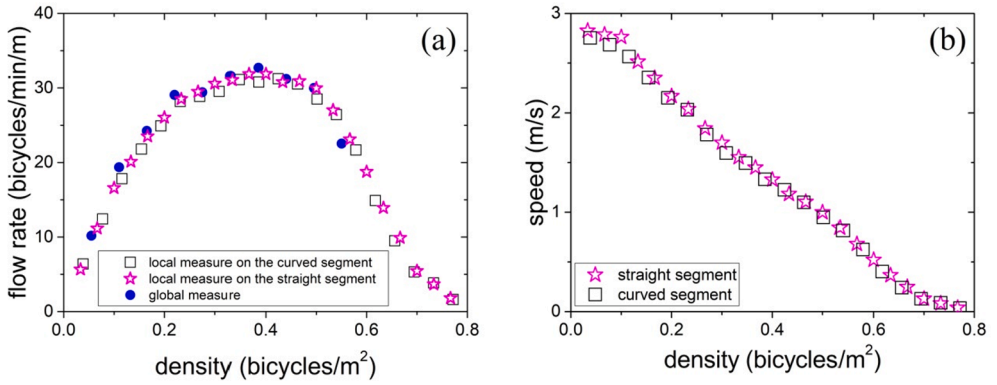

Fig. 11. Fundamental diagram of the local and global measure in experiment set II: (a) Flow rate and (b) speed, both as a function of density.

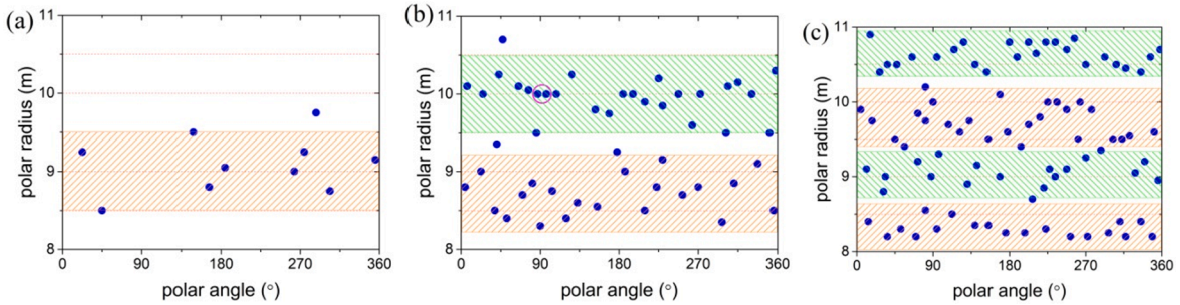

Fig. 12. Cyclist location snapshots in polar coordinates. (a) $N = 10$, (b) $N = 50$, (c) $N = 90$. Although some points appear very close to each other (e.g., red circle in panel b), the difference in polar angle between the two points is 9.75° and their distance is 1.7 m, which exceeds the size of a bicycle. The shaded rectangles roughly indicate the lanes.

$$\langle v_i(t) \rangle = \frac{\sum_{N_l(t)} v_i(t)}{N_l(t)} \tag{4}$$

where $N_l(t)$ is the bicycle number in the measured area at time t and S_l is the size of the measured area. For the measured area, we choose the middle 120° sector on the semi-circle segment and the middle 10-m-long section on the straight segment.

Fig. 11a shows that on the playground track, the flow rate-density relationship on the curved segment is consistent with that on the straight segment, and the fundamental diagram of the local measure is in consistent with that of the global measure. The free speed in the curved segment is approximately 2.7 m/s, only slightly lower than that on the straight section (~2.8 m/s) (Fig. 11b), as the cyclists do not accelerate too much on the straight segment to avoid deceleration on the curved section. The cyclist behavior on the straight and semicircle segments is therefore similar.

To determine why the flow rate remains essentially constant across a wide range of densities on the wide track, we plotted snapshots of the location (i.e., head) of each cyclist in polar coordinates (Fig. 12). The bicycles were staggered so that the space between them could be used more efficiently on the wide track. With increasing global density, the cyclists gradually formed an increasing number of lanes. Here a lane is defined as a radial range in which the radial locations of the bicycles were intensively distributed. When the density was not large, the lane width was approximately equal to 1 m, see, e.g., Fig. 12a and b. Specifically, all of the cyclists moved around a polar radius of 9 m in the 10-bicycle experiment (Fig. 12a). When the number of bicycles increased, the cyclists segregated into two lanes around polar radii of 9 m and 10 m (Fig. 12b). More lanes formed with an increasing number of bicycles (Fig. 12c), which was ultimately limited by the 3-m track width. As the density increased further, the lane width decreased, see, e.g. Fig. 12c. A typical value of bicycle width w_{bic} was about 0.6–0.75 m. Therefore, on a 3-m wide track, there was an approximate maximum of 4–5 lanes.

To quantify the above phenomenon, we introduce a weight density similar to Helbing et al. (2007):

$$f_w(D_r) = \sum_i e^{-\beta|D_i - D_r|} \tag{5}$$

where D_i is the distance between cyclist i and the track center (polar radial distance) (Fig. 1), D_r is the polar radial distance between location r and the track center, and β is a parameter set to 0.2. The summation index is the cluster degree in the radial direction. Lane number is defined as the number of peaks in the weight density function in the polar radial direction. We extract every local maximum

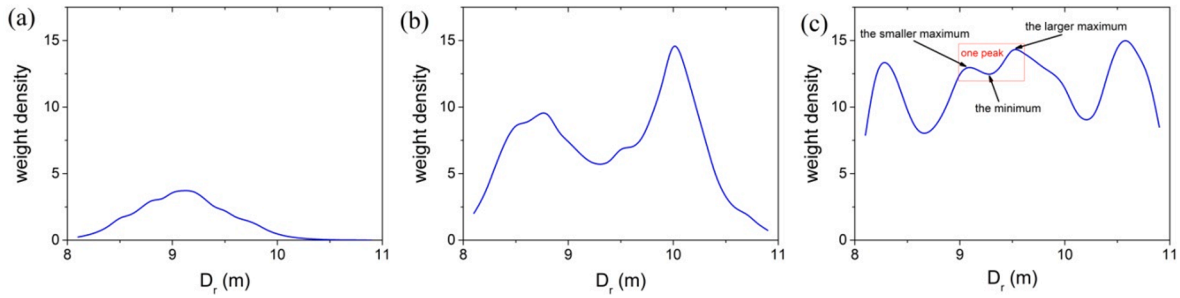

Fig. 13. Weight density in the polar radial direction. (a) $N = 10$, (b) $N = 50$, (c) $N = 90$.

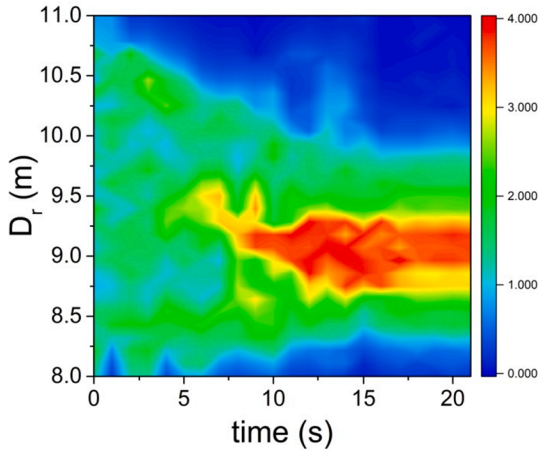

Fig. 14. Evolution of weight density in the polar radial direction in a 10-participant experimental run on the ring-shaped track.

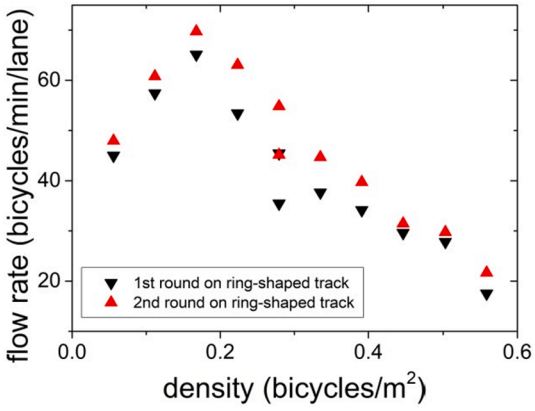

Fig. 15. Flow rate per lane versus density.

and local minimum on the curve of weight density (Fig. 13). Then, two successive maximum values and the minimum value between them are compared. If the ratio between the minimum and the smaller maximum is larger than a threshold ϑ, these two maximum values are considered as one peak with the larger maximum value (the smaller maximum and the minimum are considered as fluctuations). Otherwise, these two maximum values are considered as two independent peaks. In this paper, the threshold ϑ is set to 0.9. Fig. 13 shows that with increasing global density, the number of peaks increased from 1 to 3 following Eq. (5), which implies that the number of formed bicycle lanes increased. The linear fitting is lane number $N_{lane} = 0.5 + 0.034N$ with $r^2 = 0.903$. Fig. 14 depicts an example of the evolution of weight density in the polar radial direction in a 10-participant experimental run on the ring-shaped track. The cyclists were initially ($t = 0$–10 s) distributed rather homogeneously on the track. After 10 s, the cyclists aggregated into a lane with $D_r = \sim 9$ m. The cyclists in other runs exhibited similar lane-aggregation behavior.

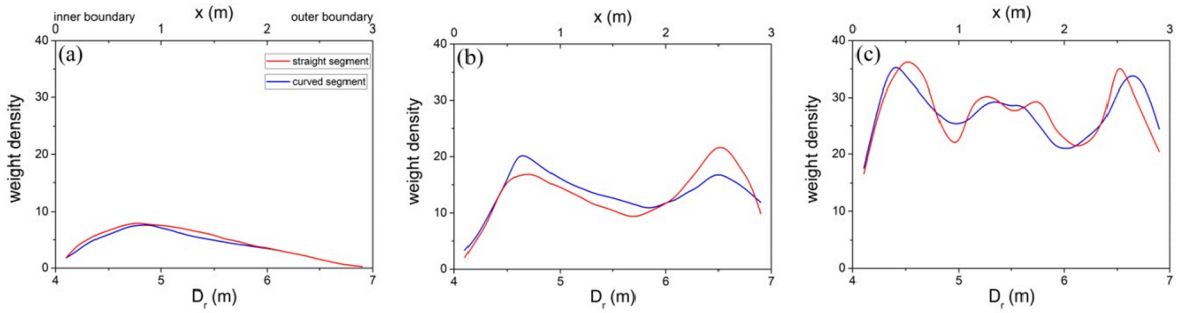

Fig. 16. Weight density on the curved segment in the polar radial direction: (a) $N = 10$; (b) $N = 50$; (c) $N = 90$.

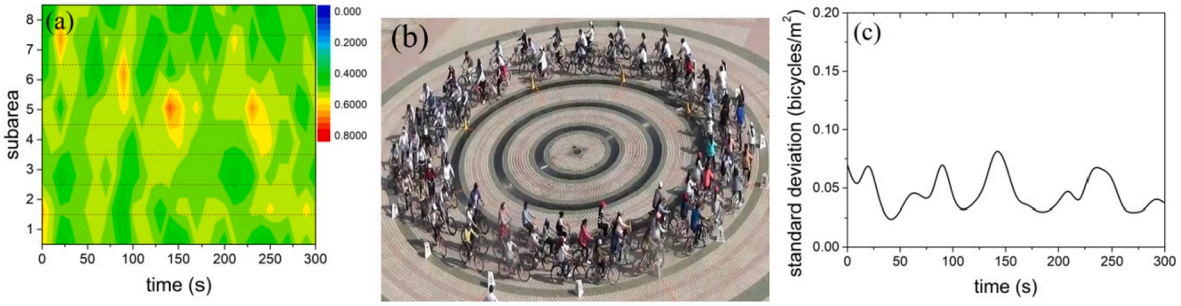

Fig. 17. Results of a 90-participant experimental run: (a) density evolution in the eight subareas, unit: bicycles/m^2; (b) snapshot photograph; (c) standard deviation of bicycle density in the eight subareas. Dashed lines represent subarea boundaries.

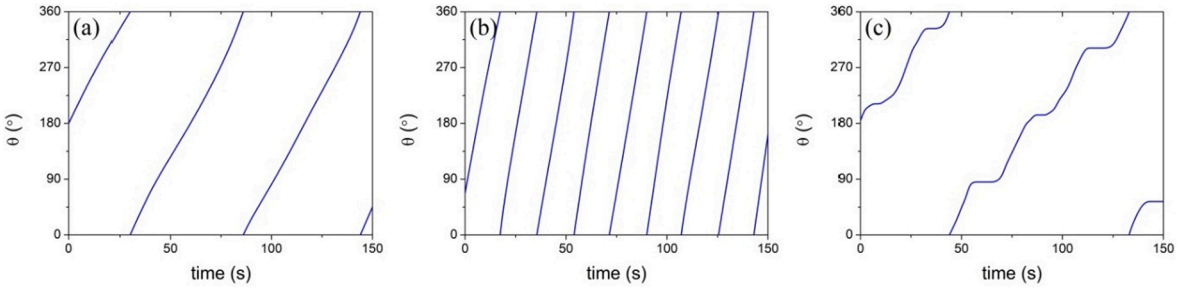

Fig. 18. Typical trajectory of the axial location of a single cyclist in experiments involving (a) 90 participants, (b) 30 participants, and (c) 100 participants.

With reference to the lane number, we calculated the flow rate per lane (defined as qw/N_{lane}); the results are depicted in Fig. 15. One can see that the flow rate per lane versus density exhibits a unimodal structure, similar to a single-file bicycle flow (Jiang et al., 2017). The cyclists responded to a wide track by forming more lanes, which allowed them to ride side by side. This increased use of space prevented the flow rate from decreasing, meaning that the flow rate remained nearly constant across a wide range of densities. However, when the number of bicycles exceeded 90, the formation of new lanes became difficult, and the flow rate therefore began to decrease.

A similar lane formation phenomenon occurred on the playground-like track. With increasing global density, the cyclists gradually formed an increasing number of lanes. All of the cyclists moved 1–1.5 m from the inner boundary in the 10-bicycle experiment (Fig. 16a). When the number of bicycles increased, the cyclists segregated into two lanes (Fig. 16b). As the number of bicycles further increased, more lanes formed (Fig. 16c). With increasing global density, the number of peaks increased from 1 to 3, which means that the number of lanes formed by the bicycles increased[2]. The linear fitting yields $N_{lane} = 0.454 + 0.032N$ with $r^2 = 0.902$.

[2] For the straight segment, D_i in Eq. (5) represents the lateral distance of bicycle i to the inner boundary and D_r is the lateral distance between location r and the inner boundary.

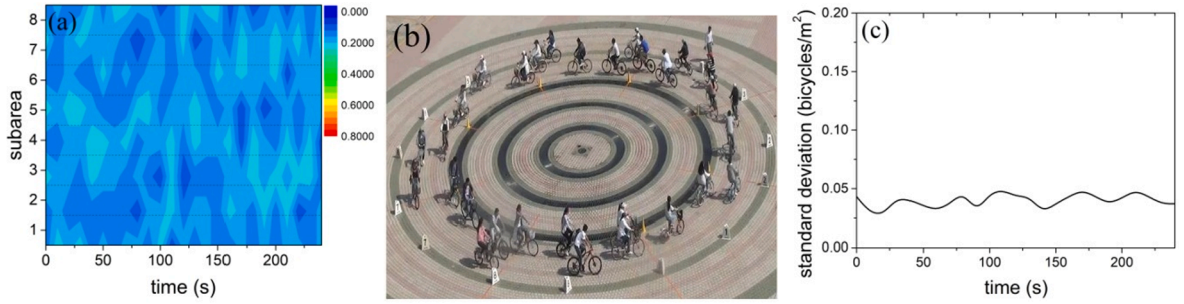

Fig. 19. Results of the 30-participant experimental run: (a) density evolution in the eight subareas; (b) snapshot photograph; (c) standard deviation of bicycle density in the eight subareas. Dashed lines represent subarea boundaries.

Fig. 20. Results of the 100-participant experimental run: (a) density evolution in the eight subareas; (b) snapshot photograph; (c) standard deviation of bicycle density in the eight subareas as a function of time. Dashed lines represent subarea boundaries and the red box represents the jam area.

3.3. Density evolution and stop-and-go traffic

In this subsection, we assess the evolution of bicycle flow at different densities on a wide track. In the free flow state, bicycles can move freely. This situation is very simple and does not require further illustration. We are mainly concerned with the saturated and congested states.

To this end, we divided the ring-shaped track into eight equal areas (Fig. 1). Here we discuss the bicycle flow results in the 90-participant experiment corresponding to the highest density in the saturation flow state. After a short transient time, the cyclists were fairly homogeneously distributed (Fig. 17). The evolution of the cyclist density in the eight subareas is shown in Fig. 17a. The cyclist densities in each subarea were approximately the same at any one time (e.g., snapshot in Fig. 17b). Randomness occasionally caused local jams (e.g., $t = 90$ s and $t = 140$ s in Fig. 17a) but the jams dissipated quickly because there was still free space on the track. Fig. 17c shows the evolution of the standard deviation of cyclist density in the eight subareas over time. The standard deviation generally remains small (~0.05 bicycles/m^2), which means that the bicycle flow is relatively homogeneous. Fig. 18a shows a typical trajectory of a cyclist's axial location. The definition of axial location is shown in Fig. 1. One can see that the trajectory is roughly linear, which means that the bicycle has a constant riding speed. Because too many bicycles were moving on the track, few cyclists had sufficient space to overtake others, and the speed remained essentially constant.

Fig. 19a shows the evolution of cyclist density in a 30-participant run, which corresponds to the lowest-density experiment in the saturation state and also shows a basically uniform distribution. Fig. 19b shows a typical snapshot photograph and Fig. 19c shows the standard deviation of cyclist density in the eight subareas. The distribution is relatively homogeneous, and the small clusters that do form quickly dissipate. Fig. 18b shows that the typical trajectory is also linear. All of the other runs corresponding to the saturation state yielded similar results.

In contrast, in the congested flow (100-participant experiment), the cyclist distribution became heterogeneous, as shown in Fig. 20a, in which stop-and-go waves spontaneously emerged. As shown in Fig. 20b, the local density in one area, indicated by a red box, was so large that the cyclists had to completely stop. The flow rate is thus a weighted average of the "stop state" (~0) and "go state" (~0.55 bicycles/s/m). The traffic jam propagated steadily upstream along the centerline between the outer and inner boundaries at a speed of approximately 1.5 m/s. The density in the jam was approximately $\rho_1 = 0.8$ bicycles/m^2. The density in the moving flow area was approximately $\rho_2 = 0.45$ bicycles/m^2, and the flow rate was $q_2 = 0.55$ bicycles/s/m. The wave propagation speed can be calculated by $q_2/(\rho_2 - \rho_1)$ and yields a propagation speed of 1.57 m/s, which is close to the 1.5 m/s observed in the experiment. This mechanism is used in vehicle traffic analysis and can also be applied to describe the stop-and-go scenario in bicycle traffic (Sugiyama et al., 2008; Tadaki et al., 2013). Fig. 20c shows that the standard deviation fluctuates around 0.125 bicycles/m^2, which is considerably larger than that shown in Fig. 17c and 19c. Similar results were observed in the second run of the 100-participant experiment; the

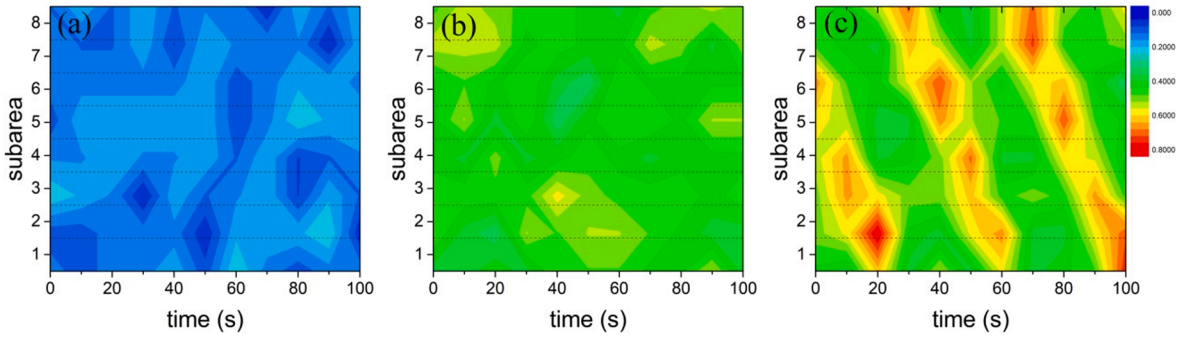

Fig. 21. Density evolution on the playground-like track: (a) 30 participants; (b) 90 participants; (c) 100 participants.

Fig. 22. Snapshot photograph on the playground-like track: (a) 30 participants; (b) 90 participants; (c) 100 participants. The red box shows a jam area.

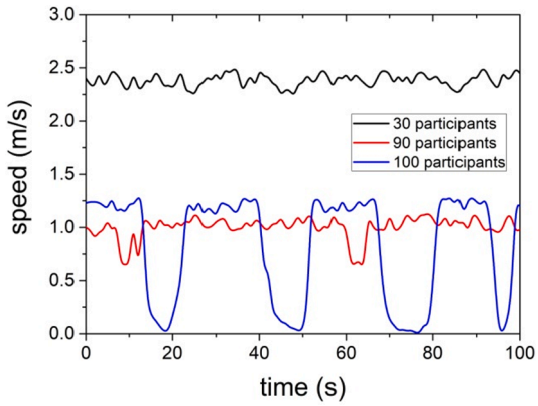

Fig. 23. Typical speed on the playground-like track.

propagation speed of the traffic jam was also approximately 1.5 m/s. Fig. 18c shows that the typical trajectory exhibits a zigzag profile due to the stop-and-go wave, which is qualitatively different from that in the saturation state.

A stop-and-go wave also emerged in the single-file bicycle experiment performed by Jiang et al. (2017). The wave propagation speed in this experiment was approximately 1.45 m/s, similar to the result we obtained in our wide-track experiment. Given that the length of a bicycle is approximately 1.5 m, the start-up delay of a bicycle is approximately 1 s. Stop-and-go traffic waves have also been observed by other researchers in studies of vehicular traffic on circular roads (Sugiyama et al., 2008; Tadaki et al., 2013). In these cases, the wave propagation speed was approximately 5.5 m/s, which is higher than that in bicycle flow. Given that the length of a vehicle plus the standstill gap is approximately 5–6 m, the start-up delay of a vehicle is also approximately 1 s. This demonstrates that the stop-and-go traffic waves that occur in bicycle flow and in vehicular flow are consistent, and are closely related to the driver/rider start-up delay.

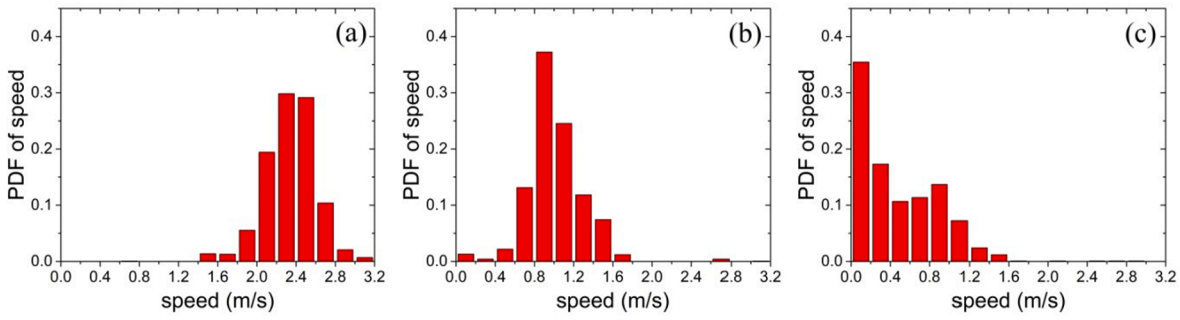

Fig. 24. Speed distribution on the playground-like track during the experiment. Number of participants (N): (a) $N = 30$; (b) $N = 90$; (c) $N = 100$. Note that PDF means probability density function.

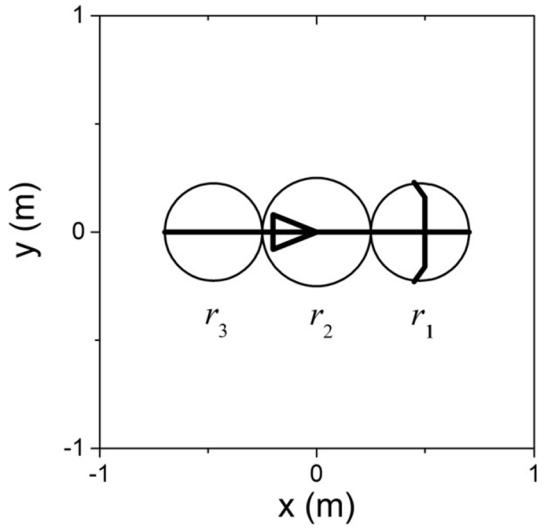

Fig. 25. Simplified structure of a bicycle/cyclist unit: three-circle shape.

We then studied the density evolution on the playground-like track (experiment set II). As before, we divided the playground-like track into eight areas (Fig. 2). The results show similar density evolutions on the straight and semi-circle segments. Fig. 21a shows the density evolution in a 30-participant run. The distribution is relatively homogeneous (Fig. 22a), and small clusters that formed in the riding process dissipated. Fig. 23 shows the typical speed of a cyclist. The riding speed was roughly constant. In the 90-participant experiment, and the cyclists were again fairly homogeneously distributed (Figs. 21b and 22b). Overall, the densities were similar along the track. Randomness occasionally caused local jams, but the jams did not propagate along the movement and rapidly dissipated. Fig. 23 shows that the typical speed was again basically constant. All of the other runs corresponding to the saturation state yielded similar results. In contrast, in the congested flow (100-participant experiment), the cyclist distribution became heterogeneous and stop-and-go waves spontaneously emerged (Figs. 21c and 22c). The propagation speed of the traffic jams was again approximately 1.5 m/s. Fig. 23 shows that the typical speed exhibits a significant fluctuating profile due to the stop-and-go wave, which is also qualitatively different from that in the saturation state.

Fig. 24 presents the speed distribution in the experiment. In the 30-participant experiment, it can be seen that the speed was highly concentrated, at approximately 2.4 m/s. However, when the participant number increased to 90, the speed retained a unimodal distribution and was concentrated at a lower value (approximate 1 m/s). However, in the 100-participant experiment, two peaks at 0 m/s and 0.9 m/s were apparent, which was attributable to the stop-and-go phenomenon.

4. Formulation of the bicycle simulation model

Modeling studies of bicycle flow on wide roads have been reported (Navin, 1994; Gould and Karner, 2009; Liang et al, 2012; Andresen et al, 2013; Ren et al., 2016; Gavriilidou et al., 2019a; 2019b; Guo et al., 2020). For example, Gould and Karner (2009) and Ren et al. (2016) developed multilane cellular automaton (CA) models and considered the lane changing behavior of bicycles. Liang et al. (2012) introduced a psychological-physical force and trajectory choice into a social force model. Gavriilidou et al. (2019a; 2019b) proposed a cyclist model from operational level, which includes mental process (path choices) and physical process (bicycle

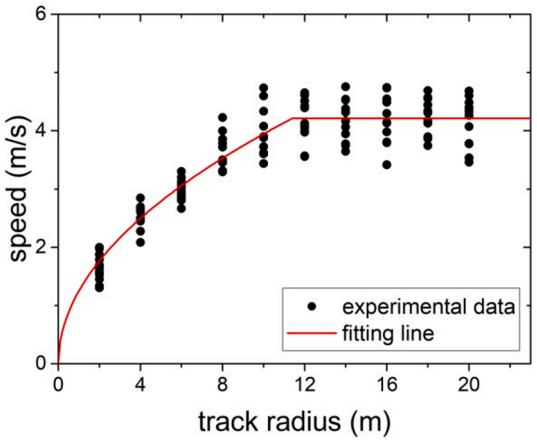

Fig. 26. Fitting line of the relationship between free speed and circle radius.

control by pedaling and steering). Guo et al. (2020) proposed and applied a heuristic-based model to simulate the mixed flow of pedestrians and bicycles.

The behavioral findings reported in Section 3.1 indicate that a bicycle flow model can depict how cyclists choose a direction and speed for their movements: cyclists change direction and speed on the basis of intelligent collision prediction rather than in response to a repulsive force. These behavioral characteristics can be captured using a heuristic-based model (Moussaïd et al., 2011; 2012).

In the real world, some bicycle road sections are curved. When the radius of the curved section is small, bicycles must typically slow down to decrease the centrifugal force. However, the centrifugal force of bicycles moving along curved roads has not been previously considered.

To address this limitation, we propose an improved heuristic-based model that accounts for centrifugal effects on bicycles. The relationship between free speed and curved radius is used to depict the target speed on tracks of different radii. A set of single-bicycle experiments were conducted to investigate the free speed of bicycles on different curvature tracks.

The model assumes that the minimum comfortable space required by a cyclist consists of three circles, as shown in Fig. 25. The radii of the front, middle, and rear circles are denoted as r_1, r_2, and r_3, respectively.

4.1. Free speed on tracks with different radii

The centrifugal effect is ignored in Guo et al. (2020). However, when a bicycle moves on a curved road with a radius R, the bicycle is subject to a centrifugal force of Mv^2/R, where M is the mass of bicycle and cyclist, and v is the bicycle speed. According to Newton's laws, the centrifugal force is equal to the friction force f_f in the normal direction of movement:

$$Mv^2/R = f_f = BMg \tag{6}$$

where B is the friction coefficient in the normal direction and g is gravitational acceleration (9.8 m/s^2). Bicycle speed has an upper bound due to the cyclist's physical ability and bicycle mechanism. The relationship between free speed v^f and curvature radius R is

$$v^f(R) = min\left(\sqrt{BgR}, v_0\right) \tag{7}$$

where v_0 is the upper bound of the free speed. In the nonlinear fitting of Eq. (7) (Fig. 26) based on a single-bicycle experiment (for more details see Appendix A), we obtain $v_0 = 4.2$ m/s and $B = 0.146$ m/s^2 with a goodness of fit $r^2 = 0.811$.

4.2. Movement model

In the model we assume that a cyclist chooses their movement direction in the range of $[\alpha_t - \varphi/2, \alpha_t + \varphi/2]$, where φ is the view range and α_t is the angle of the target movement direction. Based on our behavioral findings, the target movement direction is set to the tangential direction of the ring for the ring track and the longitudinal direction for the straight track. This modified model assumes that the cyclist wishes to move at a target speed $v^f(R)$. For all of the candidate directions α in the view range, the cyclist evaluates the distance to the first collision with other cyclists and boundaries, denoted as $f_1(\alpha)$ and $f_2(\alpha)$, respectively. If the cyclist will collide with another cyclist along the candidate direction α after time Δt, $f_1(\alpha)$ is set to $f_1(\alpha) = v^f(R)\Delta t$. Note that our model supposes that cyclists assume that other cyclists do not move[3]. In contrast, if the cyclist will not collide with anyone along the direction α or $f_1(\alpha)$ exceeds a

[3] If cyclists assume that other cyclists move with current speed, the model will overestimate the flow rate, see Appendix B.

Table 4
Parameter values of bicycle characteristics.

r_1 (m)	r_2 (m)	r_3 (m)	φ (°)	d_m (m)	a_a (m/s^2)	a_d (m/s^2)
0.225	0.25	0.225	180	5	3	6

Table 5
Calibrated parameter values.

Parameter	Interval (minimum/maximum)	Calibrated parameters in this paper	Calibrated parameters in Guo et al. (2020)
τ_1 (s)	0.00/2.00	0.75	0.75
τ_2 (s)	0.00/2.00	0.50	0.50
τ_3 (s)	0.00/2.00	0.10	0.10
τ_4 (s)	0.00/2.00	0.10	0.10
T_c (s)	0.00/2.00	0.25	0.15

threshold d_m, then $f_1(\alpha)$ is set to $f_1(\alpha) = d_m$. Similarly, $f_2(\alpha)$ is calculated by $f_2(\alpha) = min\left[v^f(R)\Delta t^{'}, d_m\right]$, where $\Delta t^{'}$ is the time needed to collide with the boundary. We then define $f(\alpha)$ as

$$f(\alpha) = min[f_1(\alpha), f_2(\alpha)] \tag{8}$$

The direction of the desired speed is obtained through

$$\alpha_d(t) = argmin\left[d_m^2 + f^2(\alpha) - 2d_m f(\alpha)cos(\alpha_t - \alpha)\right] \tag{9}$$

which can reflect the direction preference behavior. The magnitude of the desired speed is given by

$$v_d(t) = min\left\{v^f(R_t), [f(\alpha_d) - vT_c]/\tau_1\right\} \tag{10}$$

which follows the observed proportional relationship between speed and gap. Here τ_1 is the relaxation time, T_c is a safe time headway, and v is the current speed. To calculate the acceleration, the vector $\overrightarrow{v_d}$ is split into two vectors, $\overrightarrow{v_{d1}}$ along the direction of $\overrightarrow{v}$ and $\overrightarrow{v_{d2}}$ vertical to $\overrightarrow{v}$. Here, $\overrightarrow{v}$ denotes the current speed vector. The acceleration is then given as

$$\frac{d\overrightarrow{v}}{dt} = \begin{cases} min\left(\left|\dfrac{\overrightarrow{v_{d1}} - \overrightarrow{v}}{\tau_2}\right|, a_a\right) \cdot \dfrac{\overrightarrow{v_{d1}}}{|\overrightarrow{v_{d1}}|} + \dfrac{\overrightarrow{v_{d2}}}{\tau_4}, & |\overrightarrow{v_{d1}}| \geqslant |\overrightarrow{v}| \quad \text{(a)} \\ -min\left(\left|\dfrac{\overrightarrow{v_{d1}} - \overrightarrow{v}}{\tau_3}\right|, a_d\right) \cdot \dfrac{\overrightarrow{v_{d1}}}{|\overrightarrow{v_{d1}}|} + \dfrac{\overrightarrow{v_{d2}}}{\tau_4}, & |\overrightarrow{v_{d1}}| < |\overrightarrow{v}| \quad \text{(b)} \end{cases} \tag{11}$$

where τ_2, τ_3, and τ_4 are the relaxation times that correspond to acceleration, deceleration, and turning, respectively, and a_a and a_d are the maximum acceleration and maximum deceleration of the bicycle, respectively. If a bicycle's circle contacts another circle, the bicycle behind will stop at once and wait for the bicycle in front to move forward.

The Euler method was used to solve the ordinary differential equation, with a time step of 0.01 s. MATLAB was used for the programming and simulation.

5. Model calibration

We use the experimental results in experiment set I for model calibration and those in experimental set II for model validation.

5.1. Calibration method

We use the relationship between flow rate and density for calibration. The calibration method follows that presented in Davidich and Köster (2012) using the genetic algorithm. The individual fitness is defined as

$$F = 1/\sum_i^{10}\left|flow_i^e - flow_i^s\right| \tag{12}$$

where $flow_i^e$ is the average flow rate in experiment set I, $flow_i^s$ is the simulated flow rate, and $i = 1$–10 is the 10 different global densities in experiment set I. The probability of selecting an individual is

$$P_l = F_l/\sum_n F_l \tag{13}$$

where F_l is the fitness value of individual l and n is the number of individuals. In the simulation, the parameters in Eq. (3) were set to v_0

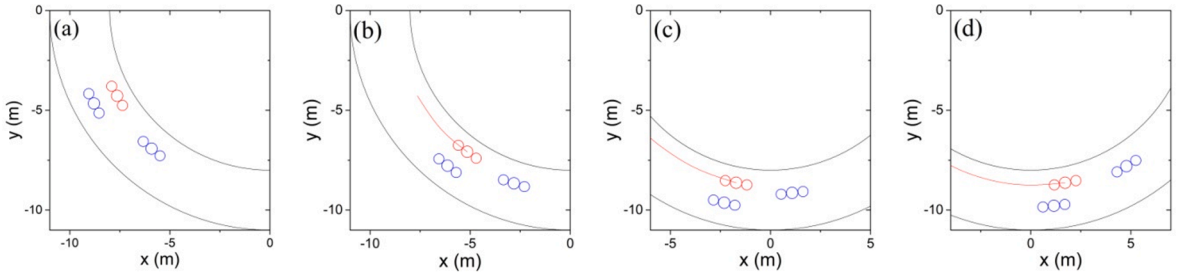

Fig. 27. Trajectory for following behavior at low density (20 bicycles).

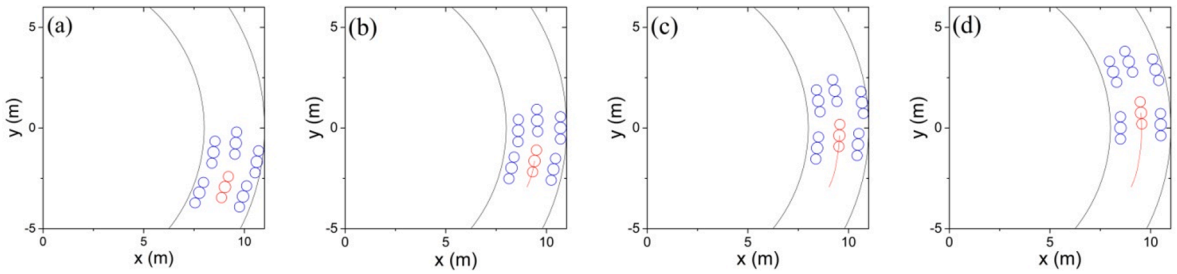

Fig. 28. Trajectory for following behavior at high density (70 bicycles).

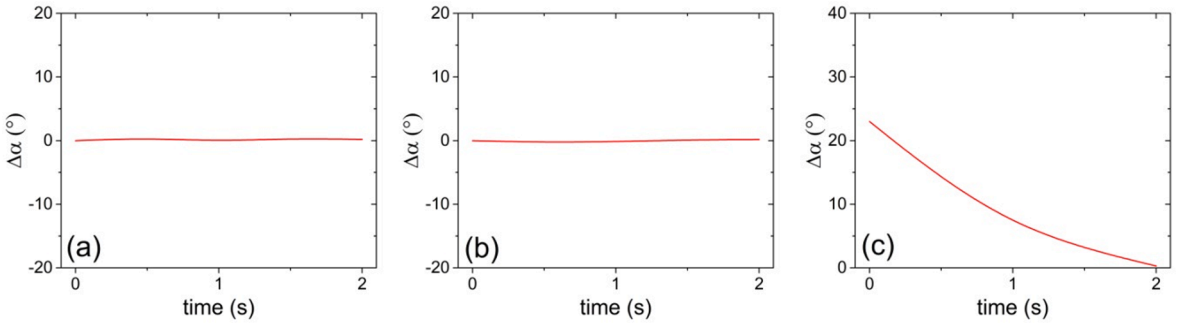

Fig. 29. Difference in angle between the target direction and movement direction (turning angle) in (a) following behavior at a low density, (b) following behavior at a high density, (c) and overtaking behavior.

$= 4.2$ m/s, $B = 0.146$ m/s^2.

Some parameters of the bicycle characteristics were implemented as in Guo et al. (2020) (Table 4), and others were calibrated, as shown in Table 5. The calibrated values are the same as those in Guo et al. (2020) except that T_c becomes larger (Table 5). A possible reason is that in pedestrian-bicycle mixed flow, cyclists reduced the safe time headway to follow other cyclists and avoid colliding with pedestrians.

5.2. Calibration results

5.2.1. Riding behaviors

The discussion in this subsection suggests that the model can reproduce the following and overtaking behaviors reported in Section 3.1. Figs. 27 and 28 show the simulated trajectories for following at low and high densities, respectively. When a cyclist follows those ahead, he or she will choose the target movement direction that has the smallest turning angle (Fig. 29a and Fig. 29b), which is consistent with the experimental results. Fig. 30 presents the simulated relationship between gap and speed during following; the results agree well with the experimental observations. Fig. 31 depicts overtaking behavior. When a cyclist wishes to overtake those ahead, he or she chooses to make a large-angled turn to move into the free space and then realigns with the tangential direction

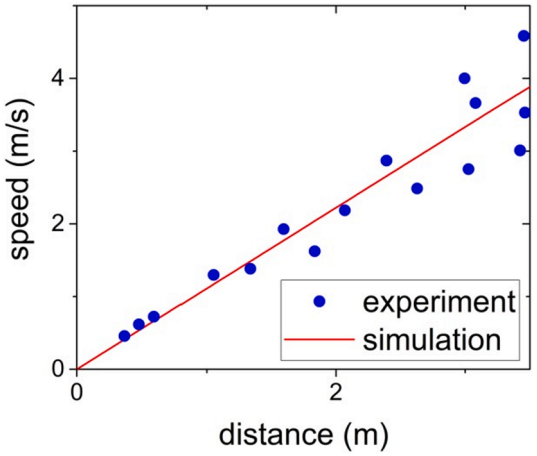

Fig. 30. Simulated relationship between gap and speed.

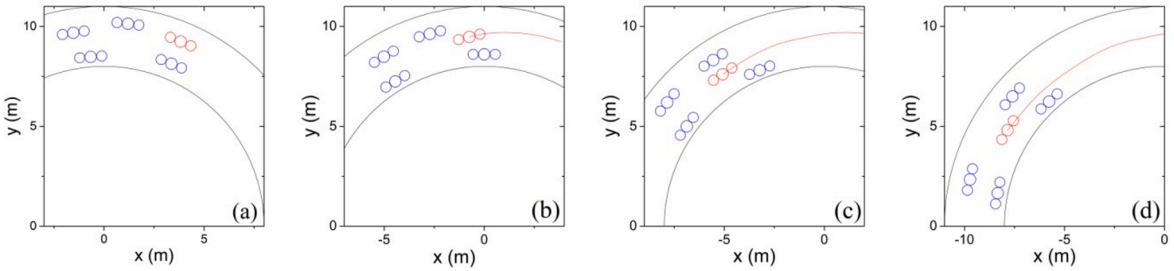

Fig. 31. Trajectory for overtaking behavior.

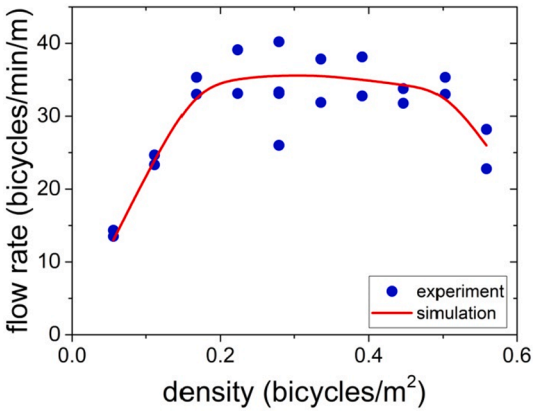

Fig. 32. Fundamental diagram obtained by simulation of a ring-shaped track.

afterward (Fig. 29c). The simulation results indicate that the proposed model can depict following and overtaking behaviors in bicycle flow.

5.2.2. Fundamental diagram, density evolution, and stop-and-go wave

Fig. 32 presents the relationship between density and flow rate. The flow rate increases with density until the density reaches 0.22 bicycles/m^2 (40 bicycles) and then becomes nearly saturated at a value of around 35 bicycles/min/m. When the density exceeds 0.5 bicycles/m^2 (90 bicycles), the flow rate sharply decreases, and stop-and-go traffic emerges. The simulation results are in good

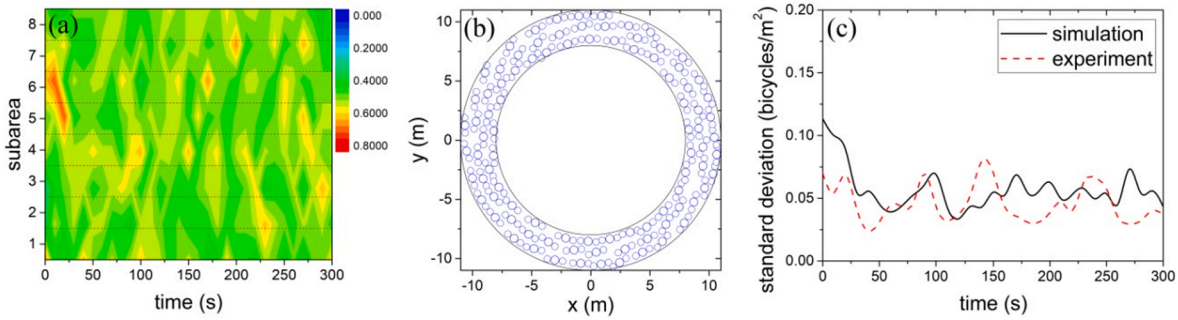

Fig. 33. Results of the 90-participant simulation run on the ring-shaped track: (a) density evolution in the eight subareas; (b) snapshot; (c) standard deviation of bicycle density in the eight subareas as a function of time. Dashed lines represent subarea boundaries.

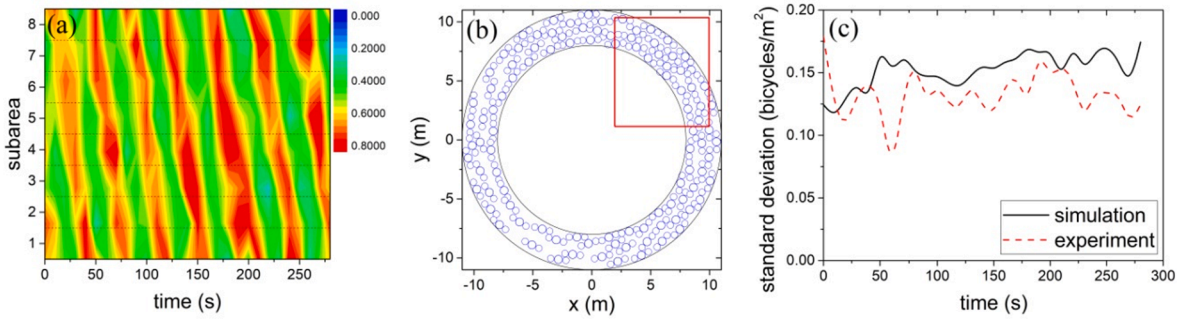

Fig. 34. Results of the 100-participant simulation run on the ring-shaped track: (a) density evolution in the eight subareas; (b) snapshot; (c) standard deviation of bicycle density in the eight subareas as a function of time. Dashed lines represent subarea boundaries and the red box represents a jam area.

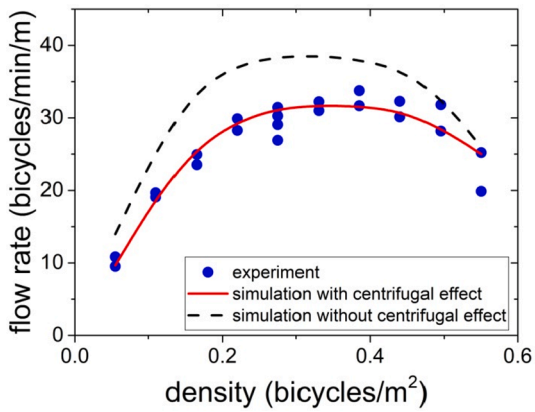

Fig. 35. Fundamental diagram obtained by simulation of the playground-like track.

agreement with the experiments. The RMSE between the experimental and simulation results is 1.327 bicycles/min/m. We performed a paired *t*-test of the experimental and simulated results, and the resulting *p*-value of 0.588 shows that there is no significant difference between these two sets of results.

We compare the cyclist distribution between the simulated and experimental results. Fig. 33 shows a typical 90-bicycle simulation result. High localized densities and small jams occasionally emerged but quickly dissipated (Fig. 33a), which is similar to the experimental results shown in Fig. 17a. Fig. 33b presents a snapshot of the location of the bicycles, showing a relatively uniform

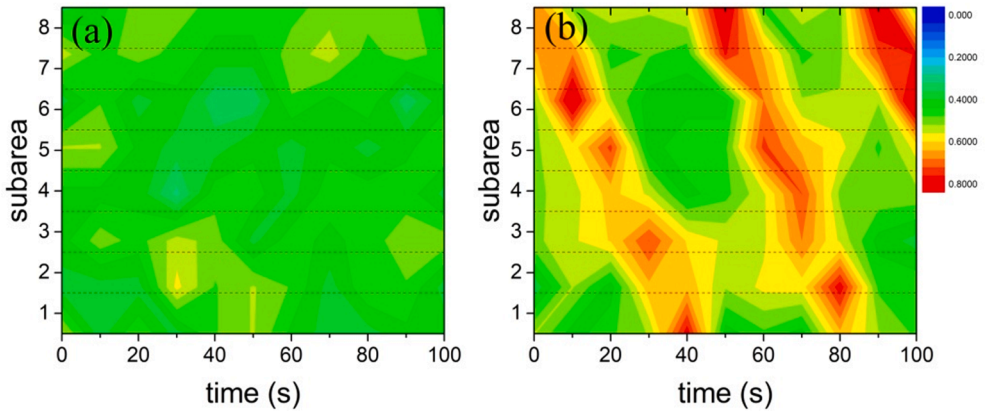

Fig. 36. Density evolution from the simulation of the playground-like track as in experiment set III: (a) 90 participants; (b) 100 participants.

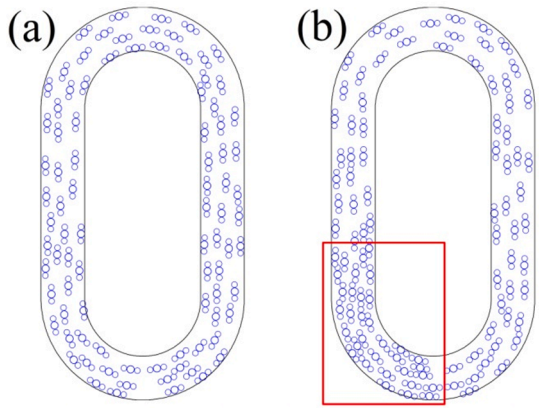

Fig. 37. Snapshot of bicycles in the simulation on the playground-like track as in experiment set III: (a) 90 participants; (b) 100 participants. The red box marks the jam area.

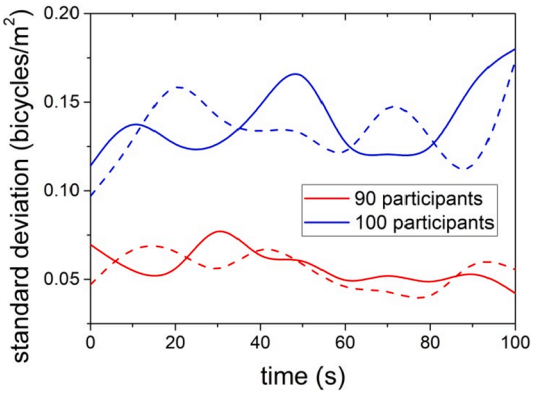

Fig. 38. Standard deviation of bicycle densities as a function of time in the eight subareas in the simulations (solid lines) and experiments (dashed line) on the playground-like track.

distribution, which is similar to the experimental results in Fig. 17b. The standard deviation of bicycle density in the eight subareas consistently remains small (Fig. 33c), which is in good agreement with the experimental results.

A phase transition occurred in the 100-bicycle simulation (Fig. 34). The jam region spread upstream, and stop-and-go traffic is observed (Fig. 34a), which is similar to the experimental results (Fig. 20a). In Fig. 34b, a non-uniform distribution emerged. The bicycles in the red box had completely stopped, which is similar to the experimental results shown in Fig. 20b. Fig. 34c shows that the

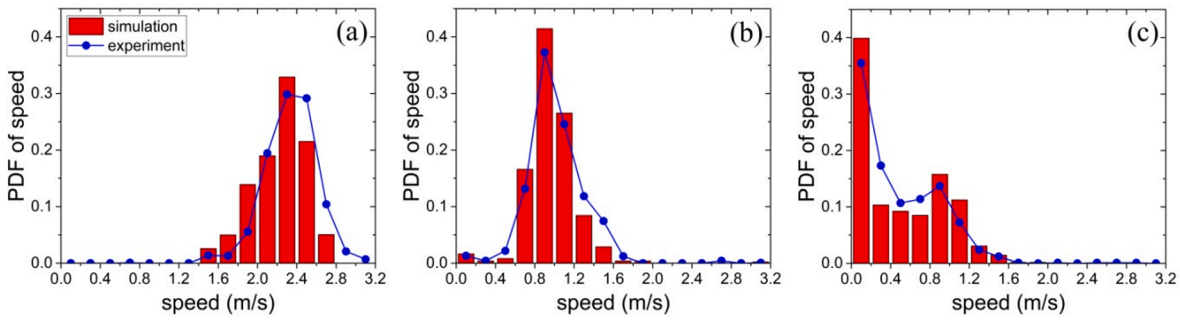

Fig. 39. Speed distribution on the playground-like track during the simulation and the experiment. Number of participants (N): (a) $N = 30$; (b) $N = 90$; (c) $N = 100$. Note that PDF means probability density function.

standard deviation of bicycle density in the eight subareas always remains high, which is in good agreement with the experimental results.

6. Model validation

In this section, experimental results on a playground-like track are used to validate the model. We set the free speed $v_0 = \sqrt{BgR}$ with $R = 7$ m, which is the radius of the outer boundary of the semicircle segment on the playground-like track. Fig. 35 presents the relationship between density and flow rate on the playground-like track. The flow rate increases with density until the density reaches 0.22 bicycles/m^2 (40 bicycles) and then becomes nearly saturated at a value of approximately 30 bicycles/min/m. When the density exceeds 0.5 bicycles/m^2 (90 bicycles), the flow rate decreases sharply and stop-and-go traffic emerges. The simulation results are also in good agreement with the experiments. The RMSE between the experimental and simulation results is 1.953 bicycles/min/m. We performed a paired t-test of the experimental and simulated results, and the resulting p-value of 0.511 shows that there is no significant difference between these two sets of results.

If centrifugal effects are ignored, the free speed is the same for both the straight track and curved tracks ($v_0 = 4.2$ m/s). The simulated flow rate (black dashed line in Fig. 35) is remarkably higher than the experimental results at low and middle densities.

Fig. 36 shows the simulation results of the density evolution on the playground-like track. Localized high densities and small jams occasionally emerged but quickly dissipated in the 90-participant simulation (Fig. 36a). The bicycles showed a relatively uniform distribution on the track (Fig. 37a), which is similar to the experimental results (Fig. 21b, 22b). Likewise, for all of the other densities in the saturation state, the simulation results are consistent with the experiments. In the 100-bicycle simulation, a non-uniform distribution emerged (Fig. 37b). The jam region spreads upstream and stop-and-go traffic is observed (Fig. 36b), which is similar to the experimental results (Fig. 21c, 22c). The simulation results for the standard deviation of bicycle density in the eight subareas are shown in Fig. 38, which are also in good agreement with the experimental range.

In the simulation (Fig. 39), it can be seen that the speed distributions are similar to those in the experiment. Thus, with increasing bicycle number, there is a unimodal distribution of speed before the stop-and-go phenomenon occurs, but the peak speed is continuously reduced. When the stop-and-go phenomenon occurs in the 100-bicycle simulation, the speed distribution contains two peaks, analogous to the experiment.

7. Conclusions

This study sheds light on bicycle flow dynamics on wide roads based on experiments and modeling. Bicycle experiments on two different types of 3-m-wide tracks were conducted to reveal the traffic dynamics of bicycle flow. The riding behaviors, including free riding, following, and overtaking, have been analyzed. It is shown that flow rate increases with increasing density within the small-density range, and remains nearly constant across a wide range of densities. The fundamental diagram thus exhibits a trapezoidal shape. We suggest that this behavior arises from the formation of more lanes with increasing global density. The extra lanes prevent the longitudinal density from increasing as quickly as in single-file bicycle flow. The results indicate a critical density of 0.5 bicycles/m^2. Below the critical density, bicycles can move relatively uniformly; above the critical density, stop-and-go waves spontaneously emerge. Based on the behavioral observations, we propose an improved heuristic-based model that considers centrifugal effects. The improved model can simulate bicycle flow on a general road with a combination of different radii. The calibration and validation indicate that the proposed model well describes bicycle flow dynamics.

The model is intended as a tool to evaluate road capacity and level of service, and to guide the design of infrastructure. As discussed in Navin (1994), the level of service (LOS) should reflect riding comfort and freedom. One LOS measure is the area occupied by a

bicycle, and the LOS criteria suggested by Navin (1994): LOS A $> 9.3\ m^2$/bicycles; LOS B $> 7.0\ m^2$/bicycles; LOS C $> 4.7\ m^2$/bicycles; LOS D $> 3.4\ m^2$/bicycles; LOS E $> 3.0\ m^2$/bicycles; and LOS F $< 3.0\ m^2$/bicycles. Thus, our model can be used to evaluate the LOS of bicycle facilities. When bicycle traffic demand is known, we can therefore calculate the area-occupancy by simulation, and thereby determine the LOS.

In our next study, we will (i) examine the impact of view on bicycle dynamics by placing a wall along the inner tack boundary to restrict participants' field of vision, (ii) further verify the proposed model with bicycle flow experiments on roads of different widths, and (iii) study the dynamics of bidirectional bicycle flow in addition to mixed flows of bicycles and electric bicycles.

CRediT authorship contribution statement

Ning Guo: Methodology, Software, Validation, Formal analysis, Data curation, Writing - original draft, Visualization, Funding acquisition. **Rui Jiang:** Conceptualization, Methodology, Writing - original draft, Supervision, Funding acquisition. **SC Wong:** Conceptualization, Methodology, Writing - original draft, Funding acquisition. **Qing-Yi Hao:** Data curation. **Shu-Qi Xue:** Data curation. **Mao-Bin Hu:** Data curation.

Acknowledgments

This work was supported by the National Key R&D Program of China (no. 2018YFB1600900), National Natural Science Foundation of China (grants nos. 71931002, 71801066, 71621001), the Research Grants Council of the Hong Kong Special Administrative Region, China (project no. 17201318), and the Fundamental Research Funds for the Central Universities (grant nos. JZ2020HGTB0021, 2016RC009). The third author was also supported by Francis S Y Bong Professorship in Engineering.

Appendix A. Single-bicycle experiment

The single-bicycle experiment was conducted on artificial straight and circular tracks on November 2, 2019 at Hefei University of Technology (Hefei, China). To demonstrate the relationship between free speed and track curvature, we choose track curvature (i.e. track radius) as the experimental variable. The length of the straight track was 21 m with an additional 10 m at both ends for bicycle acceleration/deceleration. Ten different circle-shaped track radii were selected between 2 m and 20 m using a 2-m interval. The straight-track boundaries were along dark floor tiles, as shown in Fig. A1. Each radius line of the circle-shaped track was marked with pasters (white points in Fig. A1). Six participants (undergraduate students, four male, two female) took part in the experiments. They were requested to ride on the track in their usual manner and were not informed of the experiments' purpose.

The full experimental procedure consisted of three steps. After one participant finished the process, another participant began riding on the track. In the first step, each participant was asked to ride counterclockwise on the 10 circle tracks, from the larger-radius track to the smaller one with two laps on each circle track. In the second step, the participant rode along the straight track twice, from left to right and then right to left. In the third step, the participant rode the circle-shaped tracks as the first step, but clockwise.

A video camera (Panasonic HC-VX980) was used to film the experiment from the 4th floor of a school building neighboring the track. The horizontal and vertical distances from the camera to the center of the straight track and circle-shaped track were 30 m and 16 m, respectively.

We extracted the bicycle speed, which can be regarded as the free bicycle speed. The average speed on the circle-shaped track with radius R is

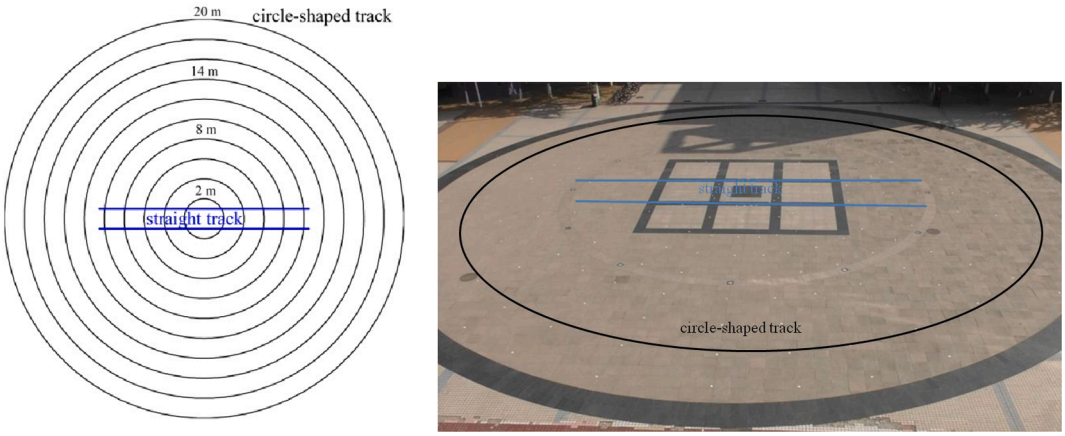

Fig. A1. Experimental field of the multi-circle track. Left: Schematic diagram; Right: photograph.

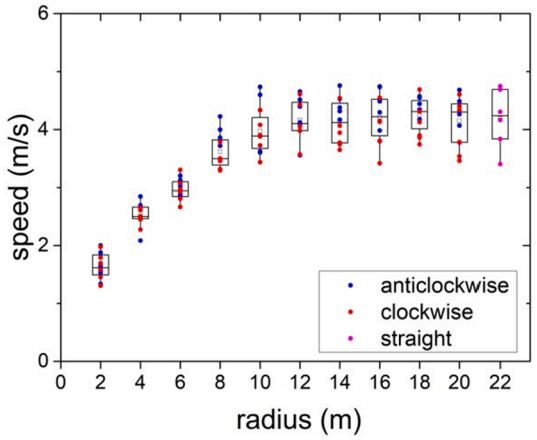

Fig. A2. Box plot of the relationship between free speed and circle radius.

$$\bar{v} = \frac{1}{N_t}\sum_{i}^{N_t}\frac{2\pi R}{T_t} \tag{A1}$$

where $N_t = 2$ is the number of riding laps and T_t is the riding time of one lap. The average speed on the straight track is

$$\bar{v} = \frac{1}{N_s}\sum_{i}^{N_s}\frac{L_s}{T_s} \tag{A2}$$

where $N_s = 4$ is the number of those riding on the straight track, T_s is the corresponding riding time, and $L_s = 21$ m is the straight track length.

As shown in Fig. A2, when the circle radius is large, the bicycle can typically maintain a free speed of approximately 4 m/s on the straight track. Until the radius decreases to ~ 10 m, the cyclist must reduce the free speed to avoid the larger centrifugal force. In the very small radius case (2 m), the bicycle can only move at around 1.5 m/s.

Appendix B. Examination of model assumption

We examined the assumption in our model concerning the evaluation of $f_1(\alpha)$. In our model, to evaluate $f_1(\alpha)$, it is assumed that cyclists expect other cyclists to remain stationary. This assumption is made because cyclists require only a short stopping distance, particularly in a congested scenario. Therefore, it is rational for cyclists to regard other cyclists as motionless. Conversely, if it is assumed that the speed and direction of other cyclists does not change, a cyclist can follow the cyclist in front of him/her at a high speed, even in a high-density scenario, which results in a high flow rate in medium/high density conditions, see Fig. B1.

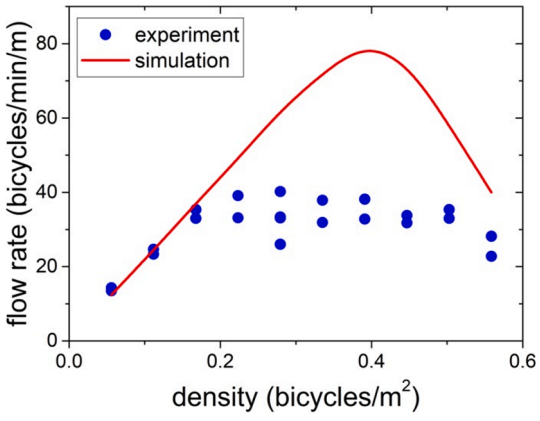

Fig. B1. Fundamental diagram. In the simulation, a cyclist assumes that the speed and direction of other cyclists remain unchanged.

References

Allen, D.P., Rouphall, N., Hummer, J.E., Milazzo, J.S., 1998. Operational analysis of uninterrupted bicycle facilities. Transport. Res. Rec. 1636, 29–36.

Andresen, E., Chraibi, M., Seyfried, A., Huber, F., 2013. basic driving dynamics of cyclists. Simulat. Urb. Mobil. 18–32.

Boltes, M., Seyfried, A., Steffen, B., Schadschneider, A., 2010. Automatic extraction of pedestrian trajectories from video recordings. In: Pedestrian and Evacuation Dynamics 2008. Springer, pp. 43–54.

Boltes, M., Seyfried, A., 2013. Collecting pedestrian trajectories. Neurocomputing 100, 127–133.

Botma, H., Papendrecht, H., 1991. Traffic operation of bicycle traffic. Transport. Res. Rec. 1320, 65–72.

Campbell, A.A., Cherry, C.R., Ryerson, M.S., Yang, X.M., 2016. Factors influencing the choice of shared bicycles and shared electric bikes in Beijing. Transport. Res. C 67, 399–414.

Cherry, C.R., 2007. Electric Two-Wheelers in China: Analysis of Environmental, Safety, and Mobility Impacts. University of California, Berkeley, CA, USA.

Davidich, M., Köster, G., 2012. Towards automatic and robust adjustment of human behavioral parameters in a pedestrian stream model to measured data. Saf. Sci. 50, 1253–1260.

Doorley, R., Pakrashi, V., Szeto, W.Y., Ghosh, B., 2020. Designing cycle networks to maximize health, environmental, and travel time impacts: an optimization-based approach. Int. J. Sustain. Transp. 14, 361–374.

Gavriilidou, A., Daamen, W., Yuan, Y., Hoogendoorn, S.P., 2019a. Modelling cyclist queue formation using a two-layer framework for operational cycling behavior. Transport. Res. C 105, 468–484.

Gavriilidou, A., Wierbos, M.J., Daamen, W., YY, Knoop, V.L., Hoogendoorn, S.P., 2019. Large-scale bicycle flow experiment: setup and implementation. Transport. Res. Rec. 2673:709–719.

Gould, G., Karner, A., 2009. Modeling bicycle facility operation cellular automaton approach. Transport. Res. Rec. 2140, 157–164.

Guo, N., Hao, Q.Y., Jiang, R., Hu, M.B., Jia, B., 2016. Uni- and bi-directional pedestrian flow in the view-limited condition: experiments and modeling. Transport. Res. C 71, 63–85.

Guo, N., Jiang, R., Wong, S.C., Hao, Q.Y., Xue, S.Q., Xiao, Y., Wu, C.Y., 2020. Modeling the interactions of pedestrians and cyclists in mixed flow conditions in uni- and bidirectional flows on a shared pedestrian-cycle road. Transport. Res. B 139, 259–284.

Helbing, D., Johansson, A., Al-Abideen, H.Z., 2007. The dynamics of crowd disasters: an empirical study. Phys. Rev. E 75, 046109.

Homburger, W.S., 1976. Capacity of bus routes and of pedestrian and bicycle facilities. Institute of Transportation Studies, University of California at Berkeley, Berkeley, CA.

Jiang, R., Hu, M.B., Wu, Q.S., Song, W.G., 2017. Traffic dynamics of bicycle flow: Experiment and modeling. Transport. Sci. 51, 998–1008.

Jin, C.J., Jiang, R., Wong, S.C., Xie, S.Q., Li, D.W., Guo, N., Wang, W., 2019. Observational characteristics of pedestrian flows under high-density conditions based on controlled experiments. Transport. Res. C 109, 137–154.

Jin, S., Shen, L.X., Liu, M.Q., Ma, D.F., 2017. Modelling speed–flow relationships for bicycle traffic flow. Proc. Inst. Civil. Eng.: Transport 170, 194–204.

Li, Z.B., Ye, M., Li, Z., Du, M.Q., 2015. Some operational features in bicycle traffic flow observational study. Transport. Res. Rec. 2520, 18–24.

Liang, X., Mao, B., Xu, Q., 2012. Psychological-physical force model for bicycle dynamics. J. Transpn. Sys. Eng. & IT. 12, 91–97.

Lin, S., He, M., Tan, Y., He, M., 2008. Comparison study on operating speeds of electric bicycles and bicycles: experience from field investigation in Kunming, China. Transport. Res. Rec. 2048, 52–59.

Liu, X., Shen, L.D., Ren, F., 1993. Operational analysis of bicycle interchanges in Beijing, China. Transport. Res. Rec. 1396, 18–21.

Mai, X., Lv, W., Wei, X.G., Song, W.G., Jiang, R., 2012. Analyzing the characteristics of unidirectional bicycle movement around a track based on digital image processing. In: 9th Asia-Oceania Symposium on Fire Science and Technology, Oct 17-20, 2012, Hefei, China.

Maibach, E., Steg, L., Anable, J., 2009. Promoting physical activity and reducing climate change: opportunities to replace short car trips with active transportation. Prev. Med. 49, 326–327.

Miller, R.E., Ramey, M.R., 1975. Width Requirements for Bikeways: A level of Service Approach. Department of Civil and Environmental Engineering, University of California, Davis.

Mohammed, H., Bigazzi, A.Y., Sayed, T., 2019. Characterization of bicycle following and overtaking maneuvers on cycling paths. Transport. Res. C 98, 139–151.

Moussaïd, M., Helbing, D., Theraulaz, G., 2011. How simple rules determine pedestrian behavior and crowd disasters. Proc. Nat. Acad. Sci. USA 108, 6884–6888.

Moussaïd, M., Guillot, E.G., Moreau, M., Fehrenbach, J., Chabiron, O., Lemercier, S., Pettre, J., Appert-Rolland, C., Degond, P., Theraulaz, G., 2012. Traffic instabilities in self-organized pedestrian crowds. PLoS Comput. Biol. 8, e1002442.

Mueller, N., Rojas-Rueda, D., Salmon, M., Martinez, D., Ambros, A., Brand, C., de Nazelle, A., Dons, E., Gaupp-Berghausen, M., Gerike, R., Gschi, T., Iacorossi, F., Int Panis, L., Kahlmeier, S., Raser, E., Nieuwenhuijsen, M., 2018. Health impact assessment of cycling network expansions in European cities. Prev. Med. 109, 62–70.

Navin, F.P.D., 1994. Bicycle traffic flow characteristics: experimental results and comparisons. ITE J. 64, 31–36.

Paulsen, M., Rasmussen, T.K., Nielsen, O.A., 2019. Fast or forced to follow: a speed heterogeneous approach to congested multi-lane bicycle traffic simulation. Transport. Res. B 105, 315–327.

Pucher, J., Buehler, R., 2008. Making cycling irresistible: lessons from the Netherlands, Denmark and Germany. Transport. Rev. 28, 495–528.

Raksuntorn, W., Khan, S.I., 2003. Saturation flow rate, start-up lost time, and capacity for bicycles at signalized intersections. Transport. Res. Rec. 1852, 105–113.

Ren, G., Jiang, H., Chen, J.X., Huang, Z.F., Lu, L.L., 2016. Heterogeneous cellular automata model for straight-through bicycle traffic at signalized intersection. Physica A 451, 70–83.

Rojas-Rueda, D., de Nazelle, A., Tainio, M., Nieuwenhuijsen, M.J., 2011. The health risks and benefits of cycling in urban environments compared with car use: health impact assessment study. Brit. Med. J. 343, d4521.

Stern, R.E., Cui, S.M., Maria, M.L.D., Bhadani, R., Bunting, M., Churchill, M., Hamilton, N., Haulcy, R., Pohlmann, H., Wu, F.Y., Piccoli, B., Seibold, B., Sprinkle, J., Work, D.B., 2018. Dissipation of stop-and-go waves via control of autonomous vehicles: field experiments. Transport. Res. C 89, 205–221.

Sugiyama, Y., Fukui, M., Kikuchi, M., Hasebe, K., Nakayama, A., Nishinari, K., Tadaki, S., Yukawa, S., 2008. Traffic jams without bottlenecks-experimental evidence for the physical mechanism of the formation of a jam. New J. Phys. 10, 033001.

Tadaki, S., Kikuchi, M., Fukui, M., Nakayama, A., Nishinari, K., Shibata, A., Sugiyama, Y., Yosida, T., Yukawa, S., 2013. Phase transition in traffic jam experiment on a circuit. New J. Phys. 15, 103034.

Wei, H., Huang, J., Wang, J., 1997. Models for estimating traffic capacity on urban bicycle lanes. Proceedings of the Transportation Research Board 76th Annual Meeting. Transportation Research Board, Washington, DC, USA.

Wen, L.M., Rissel, C., 2008. Inverse associations between cycling to work, public transport, and overweight and obesity: findings from a population based study in Australia. Prev. Med. 46, 29–32.

Wierbos, M.J., Knoop, V.L., Hänseler, F.S., Hoogendoorn, S.P., 2019. Capacity, capacity drop, and relation of capacity to the path width in bicycle traffic. Transport. Res. Rec. 2673, 693–702.

World Health Organization, 2009. Amsterdam Declaration. Third High-Level Meeting on Transport, Health and Environment. Amsterdam, Netherlands.

World Health Organization, 2011. Health in the green economy: Health co-benefits of climate change mitigation – Transport sector. Geneva, Switzerland.

Wu, F.Y., Stern, R.E., Cui, S.M., Maria, M.L.D., Bhadani, R., Bunting, M., Churchill, M., Hamilton, N., Haulcy, R., Piccoli, B., Seibold, B., Sprinkle, J., Work, D.B., 2019. Tracking vehicle trajectories and fuel rates in phantom traffic jams: Methodology and data. Transport. Res. C 99, 82–109.

Xu, K.M., 1992. Non-motorized transport in Shanghai. The World Bank, Washington DC.

Yang, M., Zacharias, J., 2016. Potential for revival of the bicycle in Beijing. Int. J. Sustain. Transp. 10, 517–527.

Zahabi, S.A.H., Chang, A., Miranda-Moreno, L.F., Patterson, Z., 2016. Exploring the link between the neighborhood typologies, bicycle infrastructure and commuting cycling over time and the potential impact on commuter GHG emissions. Transport. Res. D 47, 89–103.
Zhang, J., Mehner, W., Holl, S., Boltes, M., Andresen, E., Schadschneider, A., Seyfried, A., 2014. Universal flow-density relation of single-file bicycle, pedestrian and car motion. Phys. Lett. A 378, 3274–3277.
Zhao, Y.X., Zhang, H.M., 2017. A unified follow-the-leader model for vehicle, bicycle and pedestrian traffic. Transport. Res. B 105, 315–327.